⁴He liquid-vapor interface below 1 K studied using x-ray reflectivity

Konstantin Penanen,[*] Masafumi Fukuto, Ralf K. Heilmann, Isaac F. Silvera, and Peter S. Pershan

Department of Physics, Harvard University, Cambridge, Massachusetts 02138

(Received 22 February 2000)

The free surface of thin films of liquid helium adsorbed on a solid substrate has been studied using x-ray reflectivity. The film thickness and interfacial profile are extracted from the angular dependence of measured interference between signals reflected from the liquid-vapor and liquid-substrate interfaces. Polished silicon wafers, chemically cleaned and passivated, were used as substrates. Results are reported for measurements for ⁴He films 35 to 130 Å thick in the temperature range 0.44 to 1.3 K. The 10%/90% interfacial width for temperature $T = 0.45$ K varies from 5.3 ± 0.5 Å for 36 ± 1.5 Å thick films to 6.5 ± 0.5 Å for 125 ± 1.5 Å thick films. The profile width at zero temperature should not differ significantly from that measured at $T = 0.45$ K. For $T = 1.22$ K, the width is 7.8 ± 1.0 Å.

I. INTRODUCTION

The study of the free surface of liquid helium encompasses two major subjects of great interest and importance. First, as for any liquid, the helium surface structure is influenced by thermal fluctuations. Second, helium is fundamentally a quantum system and the surface is affected by zero-point motion.

Until the (relatively) recent advance of surface-sensitive techniques most studies of solid surfaces and all studies of liquid surfaces were limited to measurements of macroscopic quantities such as surface tension. Indeed, only with the development of intense synchrotron radiation sources could comprehensive and essentially direct measurement of surface structure of a variety of both simple and complex fluids be performed.[1–4]

For simple liquids, at temperatures ≈ 300 K, the interfacial structure can be adequately described by a thermal capillary wave model in which the dominant contribution to the surface width is due to thermally induced surface height fluctuations. In the case of liquid helium at low temperatures, the thermal capillary wave contribution to the surface width becomes small in comparison with the contribution due to zero-point fluctuations, which are generally believed to be the dominant source of broadening for the free surface of ⁴He. Most theoretical estimates for the profile width (length over which the density changes from 90 to 10 % of the bulk value) at $T = 0$ range between 2.5 and 6.5 Å.[5–14]

A number of physical phenomena of interest depend on the width of the interface between helium and its vapor. These include particle scattering off the surface of liquid helium,[15,16] and phenomena related to the existence of atomic,[17–23] and electron[24,25] bound states at the helium surface. The results we present can thus be compared with predictions based on either the theoretical estimates of the width, or on calculations based on experimental measurements of the surface excitation spectra. Experimental methods measuring surface excitation spectra include neutron scattering[26–29,14] and scattering of rotons and high-energy phonons.[30–32]

The only two direct methods capable of measuring helium interfacial profile width reported so far are the x-ray specular reflectivity method,[33] employed in the current work, and visible light ellipsometry.[34] The accessible range of the prior measurements was limited to temperatures above 1.1 K, which necessitated use of theoretical models to extract zero-temperature profile width.

Here we present experimental x-ray reflectivity data on the helium-vapor density profile which extends the temperature range of the measurements down to 0.45 K, where thermal contributions become small. In this article we present a result for the intrinsic, or zero temperature, surface profile of helium which differs from the earlier x-ray study by Lurio *et al.*, and is in essential agreement with theory.[6,7,9,11,12] The differences are due to the improved characterization of the substrate surface and a deeper understanding of how the helium-substrate system must be treated to extract meaningful information. As a consequence we also present a detailed description of the substrate.

This paper is organized as follows. Section I will proceed with a brief theoretical and experimental introduction. Section II will describe the model system. Section III will introduce the principle behind the x-ray reflectivity method. Section IV deals with the preparation and characterization of the substrates necessary for these studies. Section V is a description of the experimental apparatus. The data acquisition procedure is detailed in Sec. VI, followed by data analysis and presentation (Sec. VII). A brief discussion and conclusions are presented in Sec. VIII.

A. Theoretical overview

Several approaches have been developed towards theoretical treatment of helium surfaces. Most of them ignore the entropic effects and deal primarily with the density distribution at $T = 0$ K. Following the work of Brouwer and Pathria[5] who based their calculation on a mean field theory with a two-body local interaction, and Cole's[35] corrections which included the contribution to the surface structure due to Atkins[36] zero-point modes (see review of early theory work in Ref. 37), the theory has by now reached a high level of sophistication. Techniques used to calculate the surface structure parameters include density functional and varia-

tional methods (including Monte Carlo calculations), as well as calculations based on experimental surface excitation spectra. Nonlocal density functional approach employed by Cheng et al.,[6] gave a 10–90 % width of ≈ 6 Å for a 40 Å thick film. Guirao et al.[7] used a density functional approach with temperature dependent parameters to obtain the surface profile in the temperature range from 0 to 4.2 K, finding 10–90 % width t of 6.5 Å at $T=0$ and ≈ 6.9 Å at $T=1.2$ K. Mackie and Woo[8] predict widths $t=3$ to 4 Å for different analytical variational methods. Epstein and Krotscheck[9] provided variational calculations for films up to 20 Å thick and obtained $t \approx 5$ Å. A subsequent work by Gernoth et al.[38] in half-space geometry gives $t=4.9$ Å for the 0 K profile. Campbell et al. extended the variational calculations to include finite temperature effects.[10] Below $T=1.2$ K, thermal broadening is found to be weak for coverages away from layering transitions. Unfortunately, calculations are performed for films up to ≈ 10 Å thick only. Pieper et al.[11] obtained values of 5 and 6 Å using two Monte Carlo variational methods. Vallés and Schmidt[39] performed variational Monte Carlo and Green's-function Monte Carlo calculations on helium slabs obtained surface widths t varying from 2.8 Å for a 3.3 Å thick film to 5.0 Å for a 25.6 Å thick film. Lewart et al.[12] predict an interface width of ≈ 6.5 Å based on simulations for a cluster of 70 atoms. Based on the variational calculations of Lewart et al.,[12] Griffin and Stringari[40] showed that the low density side of the interface contains inhomogeneous dilute Bose condensate with almost 100% population of atoms in a single-particle state at $T=0$ K. Tamura[14] uses Fermi function density profile in a model where the ripplon spectrum is modified by surface diffusiveness. The surface width cited is $t=2.65$ Å.

To summarize, controversy about the width of the helium-vapor interface has not been resolved. Most theoretical calculations and indirect (neutron scattering) experimental data suggest widths between 2.5 and 6.5 Å whereas the two direct measurements by Osborne[34] and Lurio et al.[41,33,42] obtain widths of the order of 9.5 Å.

This work attempts to draw a comprehensive picture of the surface structure by providing data on the profile width as a function of both temperature and film thickness independently. With this in mind, we can classify contributions to the profile width of four types. Thickness and temperature independent, or ''intrinsic'' profile includes contributions from finite electron cloud size and incoherent short-length-scale zero-point motion. Experimental probes with small in-plane coherence length should detect this width. Thickness dependent, temperature independent contributions are due primarily to long-length-scale zero-point modes of ripplons. The third type, thickness and temperature independent, has two contributions; thermally excited capillary waves (ripplons) and the effects of bulk mode excitations interacting with the surface. Since thermally excited capillary waves are the only excited modes affecting the surface in the temperature range below 1.2 K, the fourth type, thickness independent, temperature dependent contributions to the profile width are probably not significant.

B. Experimental overview

Several classes of experiments have provided direct or indirect knowledge about the ^{4}He surface structure. X-ray specular reflectivity measurements by Lurio et al. provided the most direct measurement of the ^{4}He profile.[41,33,42] The interfacial 10–90 % width was found to be 9.1 ± 1 Å for a film of 215 Å thickness at $T=1.13$ K, and the measurements were performed in the temperature range from 1.1 to 2.2 K. Although data on several film thicknesses were taken, the amount of helium in the cell was kept constant and the temperature and thickness dependencies of the surface width were coupled. Analysis of the data was performed on the assumption that the helium-vapor and substrate-helium interfaces were not correlated. Another assumption was that reduced substrate reflectivity at small q_z was due to a hydrocarbon layer and not due to long-range surface height variations. We will argue below that the two assumptions Lurio et al. made in analyzing the data are debatable. The implications of this for the conclusions on the ^{4}He liquid-vapor interface will be discussed.

The other essentially direct measurement of the integrated width is due to Osborne,[34] who performed ellipsometric measurements. Deviations from the ideal (Fresnel) reflectivity of light at and near the Brewster angle allows one to extract the information on the surface width assuming the shape of the interface is known. Osborne assumed a Fermi function profile and found the 10–90 % width to rise slightly between 1.4 and 2.1 K with an average value of 9.4 Å at 1.8 K.

Specular reflectivity of ^{4}He atoms incident on a ^{4}He surface was measured by Nayak et al.[15] as a function of incident angle and momentum and was analyzed in terms of a model in which the effective Schröedinger equation for the incident atom is derived from a separable Hamiltonian. The interfacial 10–90 % width was extracted to be 4 Å at $T=0.02$ K. Several reservations about this value can be presented. First, the reflectivity is overly sensitive to the low-density vapor side of the profile, where the atom spends most of the time. Second, the incident atom in the model is treated as distinguishable from the ^{4}He atoms of the surface.

Berkhout et al.[16] studied quantum reflection of spin-polarized hydrogen (H↓) atoms from a concave ^{4}He-coated mirror. The temperature-dependent loss factor was attributed to thermally populated ripplons (dynamic roughness). Scattering of ^{3}He atoms from a free ^{4}He surface were performed by Edwards et al. Neither the H↓ nor the ^{3}He scattering measurements claimed to measure the interfacial width. However, this technique might possibly yield useful information. For example, Krotscheck and Zillich[43] explicitly included interaction of the incident atom with the surface excitations in their calculations of ^{3}He and hydrogen scattering from a film of ^{4}He adsorbed on substrates of various strengths.

Conceptually similar to the atomic scattering are experiments which study atomic bound states. Most recently, interest was shown in the possibility that there is more than one bound state of ^{3}He at a ^{4}He free surface (see the comprehensive review by Hallock[44]). Abnormal behavior of the ^{3}He-^{4}He mixture surface tension at low temperatures where the measured surface tension decreases with decreasing temperature was first found by Atkins and Narahara[45] and explained by Andreev[46] as being related to the existence of a surface bound state for the ^{3}He atom. The simple reasoning behind such an assumption (see Ref. 47) is that ^{3}He has

lower mass and thus larger zero-point motion than ⁴He. In the presence of a surface, a ³He atom would be expelled from the liquid side, but Van der Waals attraction would bind it to the surface. The exact form of the potential well would depend strongly on the structure of the helium-vapor interface. Theory predicts[48–51] that for a large enough interfacial width, at least two bound states would be possible even for finite ³He coverage. Crossover from populating the lowest bound state to the second as ³He coverage increases would lead to a step in heat capacity and affect NMR relaxation. Recent heat capacity measurements by Gasparini et al.[17,18] and NMR by Hallock et al.[19,20] are consistent with the existence of the second layer, but are not conclusive. Further measurements of this type may provide an estimate of the local surface density profile width. Other systems of atoms bound to free helium surface for which the binding potential is sensitive to the density profile include spin-polarized hydrogen H↓,[21–23] which has been shown to sustain a two-dimensional (2D) Bose quasicondensate[23].

Extensive literature exists on electronic bound states on helium surface. In the idealized model of an abrupt interface, a single electron is bound to the helium surface through the image potential

$$V(z) = -\frac{\epsilon-1}{4(\epsilon+1)}\frac{e^2}{z}. \tag{1}$$

To model nonabrupt liquid-vapor interface, a parametrized potential of a similar form

$$V(z) = \begin{cases} -\dfrac{\epsilon-1}{4(\epsilon+1)}\dfrac{e^2}{z+b}, & z>0, \\ V_0, & z<0 \end{cases} \tag{2}$$

with empirical parameters b and V_0 has recently been used. Cheng et al.[52] were able to recalculate the effective potential from the experimental profile by Lurio et al.[33,42] and found essential agreement of such potential with the experimental data on electron surface spectra and escape rates.[24,25] Cheng et al. noted that a 10% increase in the profile width would weaken the ground state energy by 1%. Since the calculated value of the ground state energy was ≈10% lower than the experimental value of Saville et al. this calculation does not provide strong support for the profile proposed by Lurio et al. One also has to note that the interface width in this case is associated with a lateral length scale of the order of the electron localization length. In the case of measurements performed by Saville et al.,[24] the electron areal density varied between 5×10^6 and 7×10^7 cm^{-2}, which corresponds to lengths of 12000–40000 Å. In contrast, the x-ray reflectivity method employed by Lurio et al. and in the current work probes the surface width over the effective x-ray coherence length along the surface which is of the order of 2000 Å.

Somewhat less direct information about the surface profile can be extracted from the analysis of elementary surface excitations. Experiments of this type were performed using neutron scattering[26–29,14] and interaction of rotons and high energy phonons with the surface.[30–32]

II. MODEL FOR HELIUM FILMS ON A SUBSTRATE

A. Equilibrium thickness

1. Saturated films

The attractive Van der Waals potential causes helium to adhere to almost all surfaces when the temperature is lowered sufficiently. Notable exceptions are some alkalis,[53,6] for which nonwetting has been reported. When enough helium is introduced to form bulk liquid phase at the cell bottom, the film elsewhere in the cell is ''saturated.'' The thickness of such film is determined by the strength of the Van der Waals attractive potential relative to the gravity field, and the height above the bulk phase.

For distances z from the substrate surface that are larger than several Å, the asymptotic Van der Waals potential, integrated over half space, produces an effective potential

$$V(z) = -\frac{a}{z^3}. \tag{3}$$

To account for the effects of relativistic retardation across films, this potential is commonly rewritten as

$$V(z) = -\frac{a}{z^3(1+bz)}. \tag{4}$$

The factor b is the inverse of the length scale where the retardation effects become important and is of the order of 1/200Å^{-1} (Ref. 54). In the current work the measurements and analysis are not sensitive to the exact form of the attractive potential and Eq. (3) is used.

Taking d as the thickness of the adsorbed film in equilibrium with a pool of liquid, uniformity of the chemical potential requires that

$$-\frac{a}{d^3} + gh = \text{const} = 0, \tag{5}$$

where h is the height above the pool. The thickness of the saturated helium film is then

$$d = \left(\frac{a}{gh}\right)^{1/3}. \tag{6}$$

In order to extract the Van der Waals constant a for this system the thickness of saturated films was measured using the specular reflectivity method. This value is calculated and used in the discussion on capillary wave contribution estimates.

2. Undersaturated films

When no bulk condensed phase exists in the reservoir, the chemical potential equilibrium determines the film thickness

$$m\left(gh - \frac{a}{d^3}\right) = k_B T \ln(P/P_{\text{sat}}). \tag{7}$$

Calculated thickness variation as a function of height h above the cell bottom for both saturated and undersaturated films is shown schematically in Fig. 1. For temperatures below $T\approx0.65$ K the total amount of ⁴He in the gas phase
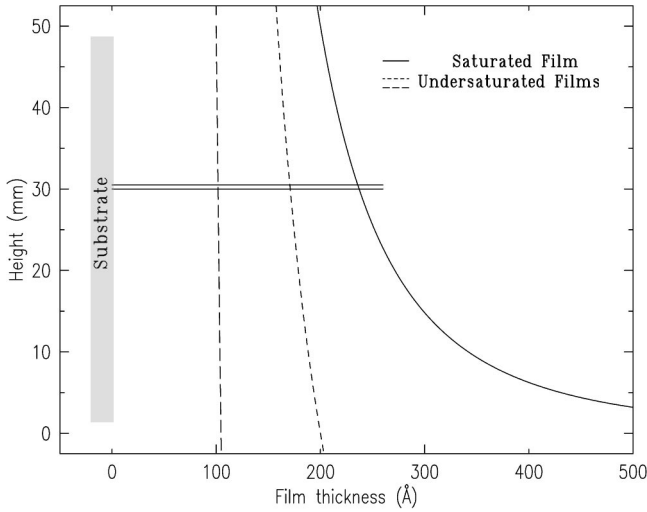
FIG. 1. Thickness of films vs height above the cell bottom for saturated and undersaturated films. Horizontal lines indicate boundaries of the x-ray beam.

becomes less than the equivalent of a monolayer and film thickness is easily maintained. Above 1 K, the temperature control needs to be maintained to within a few millikelvin to avoid film thickness variations.

B. Thermal capillary wave theory

1. Free surface

The free surface of a liquid supports collective excitation modes. The simple ripplon model described below has been verified experimentally by measuring the spectrum of collective excitations with neutron scattering (see, for example, Refs. 26,27,55) For a deep pool of liquid the surface excitation (ripplon) spectrum can be described in general (see, for example, Ref. 37, and references therein) as

$$\omega^2 = gk + \frac{\gamma}{\rho}k^3, \tag{8}$$

where ω is the ripplon frequency and k is the wave vector. The first term is due to gravity g, the second due to surface tension γ. Contribution from the two become equal for $k^2 = g\rho/\gamma$. For ^{4}He at low temperatures (0 K limit), surface tension $\gamma = 0.37$ erg$\times$cm^{-2} (Ref. 56), density $\rho = 0.145$ g $\times$cm^{-3}, and the crossover wavevector $k = 20$ cm$^{-1} = 2.0 \times 10^{-7}$ Å^{-1}. The x-ray measurements have a characteristic long-wavelength cutoff due to limited resolution at $q_{min} \approx 2 \times 10^{-3}$ Å^{-1}, and thus the gravity term in the case of free surface of bulk helium would be of no significance for the x-ray measurements.

The measured roughness can be expressed as

$$\langle \sigma^2 \rangle = \sum_i \langle A_i^2 \rangle, \tag{9}$$

where A_i is the amplitude of the ith mode. From the equipartition theorem in the classical case the amplitude can be calculated using

$$\frac{1}{2}(\gamma k_i^2 + \rho g)\langle A_i^2 \rangle XY = \frac{1}{2}k_B T, \tag{10}$$

where XY is a macroscopic sampling area. Bose-Einstein statistics needs to be employed for the modes where $\hbar\omega \gtrsim k_B T$. In this case, the right side of Eq. (10) becomes $\hbar\omega/[1 - \exp(-\hbar\omega/k_B T)]$. Substituting integration for the discreet counting of modes, Eq. 9 can be rewritten as

$$\langle \sigma^2 \rangle = \int \int_{\mathbf{k}} \langle A^2(k) \rangle \frac{XY}{(2\pi)^2} d^2\mathbf{k}. \tag{11}$$

With the mode amplitudes calculated using Eq. (10), the expected roughness can be expressed as

$$\langle \sigma^2 \rangle = \int \int_{\mathbf{k}} \frac{\hbar\omega}{e^{\hbar\omega/k_B T} - 1} \frac{1}{\gamma k^2 + \rho g} \frac{d^2\mathbf{k}}{(2\pi)^2}$$
$$= \int_{|k|} \frac{kdk}{2\pi} \frac{1}{\gamma k^2 + \rho g} \frac{\hbar\omega}{e^{\hbar\omega/k_B T} - 1}, \tag{12}$$

where $\omega = \omega(k)$ is given by Eq. (8).

2. Modifications due to the presence of a substrate

For thin films, the effect of the substrate is twofold. First, the presence of a hard wall imposes the boundary condition that the normal component of the helium velocity be zero at the surface. Equation (8) becomes

$$\omega^2 = \left(gk + \frac{\gamma}{\rho}k^3\right)\tanh(kd). \tag{13}$$

More significant for our purposes is that the attractive Van der Waals potential acts as a local gravity field with strength $d\phi/dz = 3a/d^4$. The Van der Waals constant a can be estimated from the equilibrium thickness of a saturated film. For a saturated film at height h above the bulk puddle, $gh = a/d_{sat}^3$, so that for an arbitrary film thickness d:

$$\frac{d\phi}{dz} = \frac{3gh}{d_{sat}}\left(\frac{d_{sat}}{d}\right)^4.$$

Typical saturated film thickness is 225 Å at 3 cm height, and the value of g in Eqs. (8), (10), and (11) must be replaced by an equivalent (effective) gravity field

$$g_{eff} = 3.9 \times 10^9 \left(\frac{d_{sat}}{d}\right)^4 \text{ cm s}^{-2}.$$

The crossover wavevector $k = \sqrt{g_{eff}\rho/\gamma}$ for which capillary (surface tension) and Van der Waals energies become comparable becomes

$$k = 3.9 \times 10^4 \left(\frac{d_{sat}}{d}\right)^2 \text{cm}^{-1} = 3.9 \times 10^{-4}\left(\frac{d_{sat}}{d}\right)^2 \text{Å}^{-1}.$$

For all films studied in this work the contribution due to Van der Waals forces needs to be taken into account. Figure 2 shows the result of numerical calculations of the thermal capillary wave contribution to the roughness as a function of temperature for a set of film thicknesses. Figure 3 shows the same contribution plotted as a function of thickness for two temperatures.
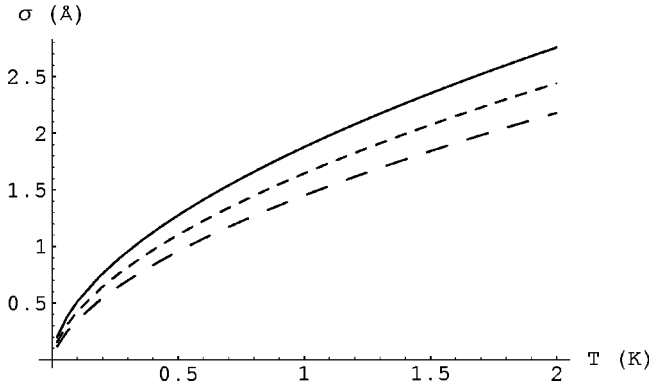
FIG. 2. Calculated thermal capillary wave contribution to the roughness as a function of temperature for film thicknesses of 200, 100, and 60 Å (top to bottom).

III. THE METHOD OF X-RAY REFLECTIVITY

A. Fresnel reflectivity

The typical geometry for an x-ray reflectivity measurement is shown in Fig. 4. Incident x rays of wavelength λ with wave vector $\mathbf{k}_{in}$ strike the surface at an angle θ and are reflected specularly. Wave vector transfer $\mathbf{q}_z = \mathbf{k}_{out} - \mathbf{k}_{in}$ is normal to the surface and has amplitude of $q_z = (4\pi/\lambda)\sin\theta$. Information about the surface structure can in many instances be extracted from the angular dependence of the specular reflectivity, i.e., reflected intensity normalized to the incident beam intensity.

X rays are scattered elastically off the electrons in the material. Such electrons can be considered essentially free since the energy of the x rays (of order 10 keV) is much larger than the electron binding energy for both helium and silicon. X rays thus probe the electron density of the interface.

For an ideally terminated surface of a material with electron density ρ and absorption length μ, reflectivity of x rays with wavelength λ can be determined exactly by solving Maxwell's equations for the incident wave with the appropriate boundary conditions.[57] Neglecting absorption and in small angle approximation, the ideal Fresnel reflectivity R_F can be expressed as

$$R_F = \left| \frac{\theta - \sqrt{\theta^2 - \theta_c^2}}{\theta + \sqrt{\theta^2 - \theta_c^2}} \right|, \qquad (14)$$
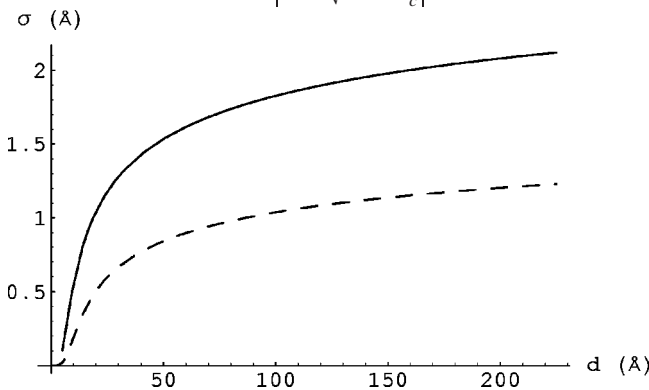

FIG. 3. Calculated thermal capillary wave contribution to the roughness as a function of film thickness for temperatures of 1.2 K (top) and 0.45 K (bottom).
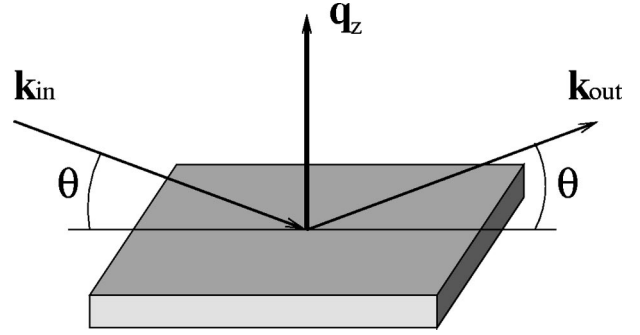

FIG. 4. X-ray reflectivity geometry.

where $\theta_c^2 = \rho e^2 \lambda^2 / \pi m c^2$, with e and m referring to electron charge and mass. Equation 14 can be rewritten in terms of the wave vector transfer

$$R_F(q_z) = \left| \frac{q_z - \sqrt{q_z^2 - q_c^2}}{q_z + \sqrt{q_z^2 - q_c^2}} \right|. \qquad (15)$$

The critical wave vector transfer $q_c = (4e/c)\sqrt{\pi\rho/m}$ is not a function of wave length, making x-ray reflectivity data presentation in terms of q_z a natural choice.

Reflectivity falls off sharply with increasing q_z, which limits the maximum accessible wave vector transfer. In the large q_z limit $(q_z \gtrsim 5q_c)$, $R_F \approx (q_c/2q_z)^4$. With $q_c = 0.0317$ Å^{-1} for silicon, 0.0077 Å^{-1} for ⁴He under vapor pressure at $T = 1$ K, and synchrotron dynamic intensity range of 10^{11}, reflectivity measurements cannot be extended beyond $q_{max} \approx 1.0$ to 1.5 Å^{-1} and often are limited further.

B. Real surfaces

If the interface has some structure in the direction normal to the surface, the reflected intensity is modified. A precise solution of such problem is quite involved, but certain approximations can be made in relevant important cases. If one is to neglect multiple reflections (which is justified by small integrated scattering cross section at larger angles) and changes to the wave vector within the interface (equally justified at larger angles), the first Born approximation can be employed.[57]

In this approximation, the differential scattering cross section is given by

$$\frac{d\sigma}{d\Omega}(q) = \left(\frac{e^2}{mc^2} \right)^2 \left| \int_{\mathbf{r}} \rho(\mathbf{r}) e^{i\mathbf{q}\mathbf{r}} d^3\mathbf{r} \right|^2. \qquad (16)$$

It can be further shown[58] that

$$R(q_z) = R_F |\Phi(q_z)|^2, \qquad (17)$$

where the surface structure factor $\Phi(q_z)$ is given by

$$\Phi(q_z) = \frac{1}{\rho_\infty} \int_{-\infty}^{\infty} \frac{d\langle \rho(z) \rangle_{x,y}}{dz} e^{iq_z z} dz. \qquad (18)$$

Density ρ_∞ refers to the bulk density; averaging is done over the coherence area which may be q_z dependent.

C. Validity of Born approximation

Equation (18) is valid when the assumptions of the Born approximation hold. The extent to which multiple reflections can be neglected is illustrated by the fact that by $q_z = 5q_c$ single scattering reflectivity is of order 10^{-4}. Also, both the coherence length along the z direction and the projection of the absorption length should be substantially larger than the thickness of the interfacial structure.

D. Off-specular scattering and background signal

In-plane inhomogeneities of the surface result in off-specular scattering. If the in-plane correlation length of these inhomogeneities is sufficiently large this scattering can appear to broaden the specular signal. This is the normal situation for bulk liquids.[59] Such scattering can have coherent components resulting, in the case of bulk liquids, in broadening of the specular signal.

E. Ambiguity of reflectivity data

The Fourier transform in Eq. (18) can in principle be inverted to extract the surface density profile. Unfortunately, the detector counts are proportional to the reflected *intensity* [Eq. (17)], and the phase information on the structure factor Φ is lost. X-ray reflectivity models do not guarantee uniqueness.[60] ''Model-independent'' methods in x-ray and neutron reflectivity rely on small q_z data where Born approximation and Eq. (18) are not valid.[61–63]

Additional difficulty arises from the fact that due to rapidly falling intensity with increasing q_z, reflectivity measurements are limited to finite maximum wave vector transfer $q_{z\max}$. Because of this, the x-ray reflectivity method is unable to discern features of size smaller than $\approx 2\pi/q_{z\max}$.

F. Interference method

Consider a two-slab model, of the type shown in Fig. 5, where the two interfaces are separated by distance d and have structure factors $A(q_z)$ and $B(q_z)$. Reflectivity from such a system will be proportional to

$$
\begin{aligned}
|\Phi(q)|^2 &= |A(q_z) + B(q_z)e^{iq_z d}|^2 \\
&= |A(q_z)|^2 + |B(q_z)|^2 + A(q_z)B(q_z)^* e^{-iq_z d} \\
&\quad + A(q_z)^* B(q_z) e^{iq_z d}.
\end{aligned} \tag{19}
$$

If the complex structure factor for one of the interfaces A is known, both the phase and amplitude of the scattering amplitude $B(q_z)$ can be extracted for Eq. (19).

IV. SUBSTRATES

The subject of this section is preparation, handling and analysis of wafers used as substrates for x-ray reflectivity measurements in the interference geometry. Although in itself the study of substrates described here does not result in significant scientific progress, the results achieved are instrumental to understanding and interpretation of helium film measurements.
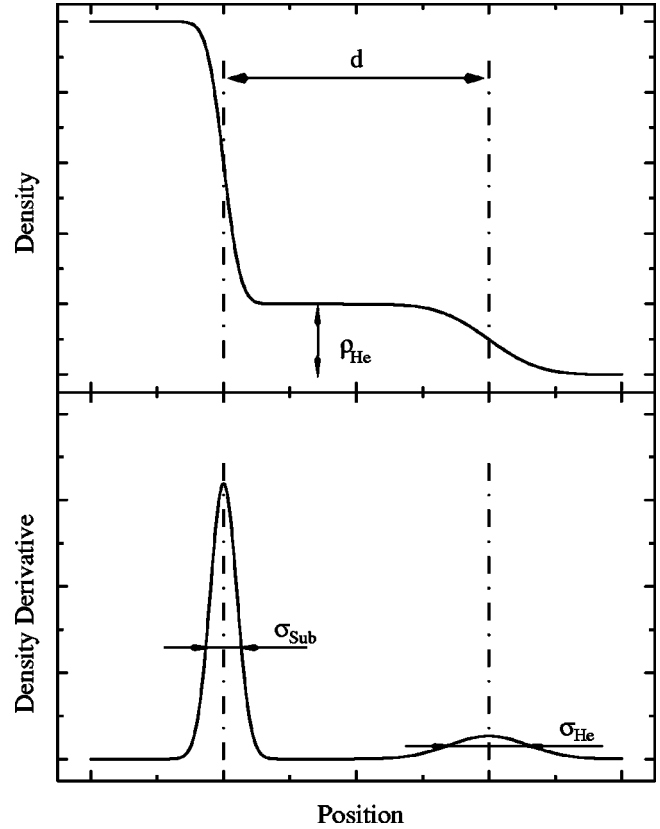

FIG. 5. Schematic representation of density profile (top) and its derivative (bottom)

A. Handling and measurement procedures

The substrates eventually used in the helium film measurements were polished Si wafers cut along the (111) plane. Several different batches were used, provided by different manufacturers[64,65] and cut to different specifications.

The substrates were preselected and analyzed at the Harvard MRSEC rotating anode facility, where as-shipped roughness and miscut were determined by x-ray techniques. Further analysis was performed using the MRSEC Scanning Electron Microscope and Atomic Force Microscope facilities.

Typical RMS roughness for substrates as shipped was 5 to 7 Å, measured by x-ray reflectivity with typical in-plane coherence legth on the order of 1000–10 000 Å. Chemical cleaning, etching, and hydrogen passivation procedures (see Sec. IV C) were applied, and the substrate was mounted inside the cell (see Fig. 6). Until the cell was completely closed, a flow of clean (boiloff) nitrogen or helium gas was maintained to finish drying the substrate and to avoid oxidation and hydrocarbon contamination. The cell was then evacuated outside the cryostat through a 77 K cold trap. Total time between the last (passivation) step of the chemical procedure and bringing the cell to a pressure of at most 10^{-4} Torr was of the order of 15 min, of which the time in air was no longer than 2 min.

The cell was continuously evacuated through a cold trap throughout the first set of reflectivity measurements. If the results of those measurements proved satisfactory, the evacuation path was sealed and the cell was mounted in the cryostat. The filling line was purged thoroughly with helium and
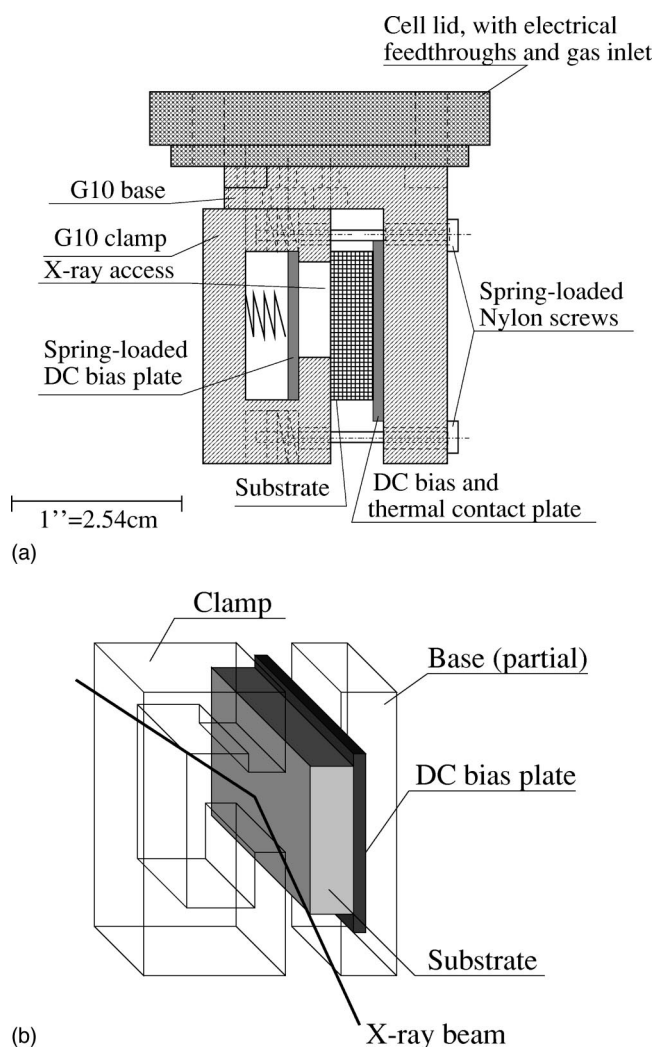
FIG. 6. (Top) Top lid of the cell with substrate holder attached. The base and the clamp of the sample holder are made of G10 epoxy. dc bias can be applied to the dc bias plates. Wiring connecting the plates to the feed-throughs is not shown. (Bottom) Schematic diagram of the substrate holder.

evacuated before the valve on top of the cell was re-opened. The cell was continually pumped out throughout the cryostat pump-out and cool down to liquid nitrogen temperatures. At that stage another set of reflectivity measurements was performed to insure that no contaminant had precipitated on the substrate surface. More measurements were performed on the substrate after the final cool-down to 4.2 K, and then to 1.1 and to 0.5 K.

B. Substrate selection

Several types of Si(111) wafers as well as some other materials were studied as potential substrates. For completeness these are discussed below, along with the problems encountered. Only the silicon substrates were used in the helium film studies.

1. Metal and metal-coated substrates

The idea to use conducting substrates was introduced after possible helium film electrostatic charging became a subject of study. Exploratory measurements were performed on a

TABLE I. Hydrogen passivation procedure. Composition of the chemicals is shown in Table II. De-ionized (18.2 MΩ cm) water was used.

	Procedure	Chemical	Time	Comment
1	Solvent cleaning	Trichloroethelene	15 min	Sonicate
2		Acetone	15 min	Sonicate
3		Methanol	15 min	Sonicate
4	Rinse	Water	1 min	
5	Basic cleaning	Clean 1	10 min	Heat to 80°C
6	Rinse	Water	1 min	
7	Acidic cleaning	Clean 2	5 min	Heat to 80°C
8	Rinse	Water	1 min	
9	Etch	10% HF	0.5 min	
10	Rinse	Water	1 min	
11	Acidic cleaning	Clean 2	5 min	Heat to 80°C
12	Rinse	Water	1 min	
13	Etch	10% HF	0.5 min	
14	Passivation	NH$_4$F	8 min	De-gas

platinum single crystal (111) substrate. Excessive roughness (>8) and figure error (macroscopic surface curvature) made measurements in the interference geometry impossible.

Another substrate, an iridium/chromium-coated silicon wafer, with suitable roughness and curvature, was nonetheless rejected. The x-ray (electron) density of that wafer was substantially larger than that of silicon and the interference contrast for adsorbed helium films was reduced significantly.

2. Thin substrates

An attempt was made to use 1.6 mm (1/16 in.) thick Si wafers. However, the stress of the mounting clamp deformed the wafer enough to create significant macroscopic curvature. All further measurements were performed with either 3.175 mm (1/8 in.) or 9.525 mm (3/8 in.) silicon substrates.

C. Chemical treatment

The substrate holder can accommodate substrates 18 to 32 mm wide and up to 45 mm long. When the wafer needed to be cut from a larger piece, the polished surface was first covered with hot wax. The cut was made with a diamond saw, after which the substrate was cleaned in toluene and sulfuric acid.

1. Chemical cleaning and hydrogen passivation

Chemical treatment was essential in obtaining contamination-free, flat substrates. The procedure of making Si(111) surfaces flat on atomic scale was introduced by Higashi *et al.*[66] Roughening of the silicon surface is attributed to the formation of amorphous silicon oxide. Preferential etching of the oxide reduces the roughness, while saturating dangling bonds of the outermost silicon layer with hydrogen passivates the surface.

Table I outlines the recipe followed. Chemicals used are listed in Table II. It is essential that the passivation solution be degassed. Residual oxygen in the passivating solution apparently reoxidizes the surface and leads to proliferation of small triangular pits.[67] In current studies degassing was

TABLE II. Chemicals used in the passivation procedure.

Substance	Content	Chemical/Brand
Clean 1	1:1:5	$NH_4OH:H_2O_2:H_2O$
Clean 2	1:1:5	$HCl:H_2O_2:H_2O$
NH_4OH	30%	Generic
H_2O_2	30%	Generic
HCl	37%	Generic
HF	48%	VLSI low particulate grade (Ref. 73)
NH_4F	40%	VLSI low particulate grade (Ref. 73)

achieved by flowing clean (boiloff) helium or nitrogen through a polypropylene disposable pipet tip into the solution for 20 min. before the substrate was placed in it and during the passivation step.

Teflon beakers were used in both etching and passivation steps. The substrates appeared hydrophobic after etching and passivation, and hydrophilic after all other steps. Note that there are no rinsing steps either before or after the passivation step.

It is important to place the wafer in an oxygen-free environment as soon as possible to avoid reoxidation. In addition, the atmosphere should be relatively free of hydrocarbons that could adsorb on the surface. After 30 min. in room air, the measured roughness can increase by as much as 2 Å. The chemical passivation procedure can be repeated if the substrate deteriorates.

2. Oxidation

Macroscopic scratches on some substrates could not be removed by the etching and passivation procedures. For these wafers, a significant improvement was achieved by oxidizing them before chemical treatment. Oxidation and annealing were performed in a vacuum furnace at temperatures up to 1050 °C in an atmosphere of 100 Torr of oxygen. Typical time of oxidation was 2–3 h. X-ray reflectivity measurements showed formation of a 500–700 Å oxide layer with roughness of the oxide-silicon interface of the order of 1 Å vs original surface roughness of 5–7 Å. This reduced roughness was preserved after the oxide layer was removed.

D. Substrate surface structure

The chemical procedure described above is known to produce microscopically flat surfaces. The presence of the hydrogen chemically bound to the dangling silicon bonds can be expected to introduce a layer of reduced density at the surface (of the order of 1 Å thick). That layer would not be visible in x-ray reflectivity measurements of a bare substrate and so, one would expect reflectivity to follow the theoretical Fresnel curve. This simplistic model does not, however, take into account possible difference between the directions of the (111) crystalline plane and that of the average polished surface (miscut). A somewhat simplified picture of that is shown in Fig. 7. In x-ray reflectivity measurements, the surface structure along the surface normal is averaged over the effective x-ray coherence area. If the x-ray coherence area is large enough so that it overlaps several steps, the x-ray reflectivity plane is the *average* surface with the scattering vector normal to it. In this ideal situation, however, the fact that
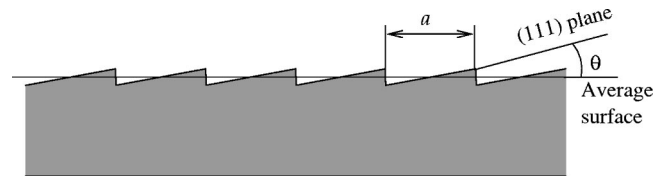

FIG. 7. Schematic representation of a surface with a miscut. For miscut angle θ and step height d, step width is $a = d/\theta$.

the height distribution around the average plane is not random (Gaussian), but rather is uniform, modifies the expected reflectivity. The difference, however, is only noticeable at larger angles (see Fig. 8). The presence of in-plane structure is also responsible for off-specular scattering. If the structure is periodic this gives rise to Bragg diffraction maxima. Note that even for an ideal substrate with interplane spacing d and zero microscopic roughness, any miscut θ will result in a r.m.s. width of at least $d/2\sqrt{3}$ as long as the coherence length is larger than the width of steps $a = d/\theta$. Silicon (111) interplane spacing is $d = 3.14$ Å and the calculated r.m.s. width for a surface with uniform miscut is $\sigma \approx 0.91$ Å. Further, a more important complication arises from the fact that the x-ray coherence length is finite and is a function of incident angle in the reflectivity geometry. This point is illustrated by the analysis of x-ray, AFM, and SEM measurements on a set of substrates, discussed below.
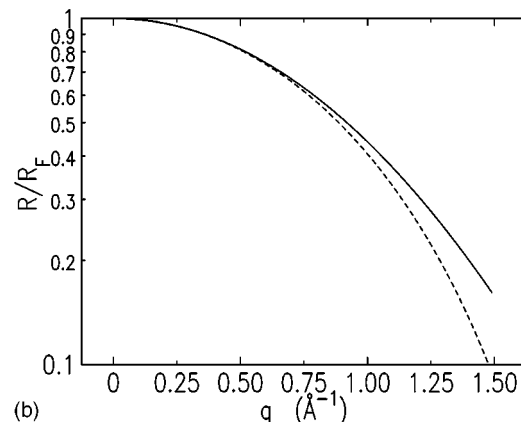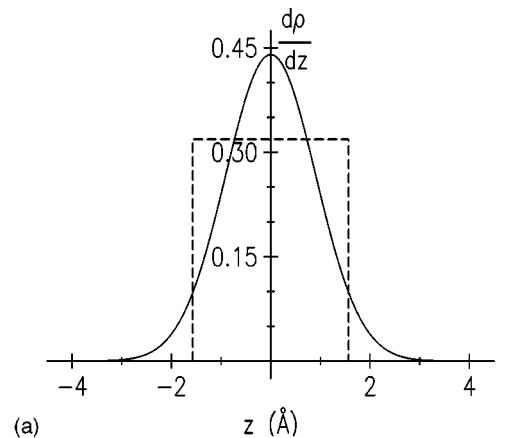

FIG. 8. Derivative of the surface density profile $d\rho/dz$ (left) and the expected reflectivity normalized to Fresnel reflectivity (right) for a substrate with uniform miscut (----). The solid line represents same for a Gaussian density distribution with the same r.m.s. width. Si(111) interplane spacing d is 3.14 Å.
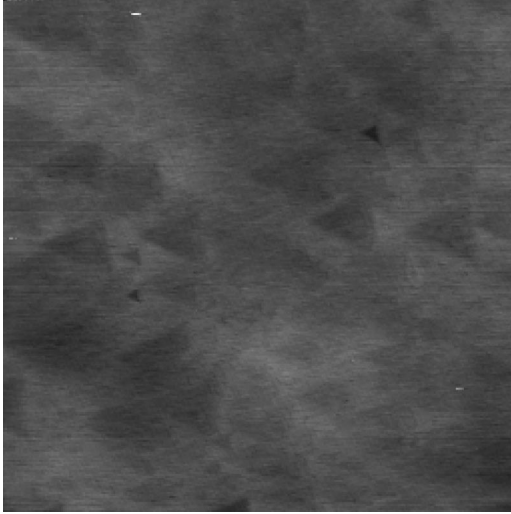
FIG. 9. AFM image of a substrate from batch A. Image size is $10 \mu m \times 10 \mu m$. Height variation from deepest to highest (dark to light) for this sample is 109 Å, with overall r.m.s. height variation of 6.76 Å.

1. Batch A, AFM

Substrate A[65] was used for some preliminary measurements. An AFM image of this substrate taken after chemical processing is shown in Fig. 9. The triangular structures in the figure are pits etched in the surface. The pits are of pyramidal form, with walls formed by the $(\bar{1}\bar{1}1)$, $(1\bar{1}\bar{1})$, and $(\bar{1}1\bar{1})$ planes. The pyramids are usually truncated by another (111) plane, so that the typical height variation at a pit is just several atomic layers. The r.m.s. height variation across the entire scanned area ($10 \mu m \times 10 \mu m$) as measured by AFM is 6.7 Å. Note that the origins of this surface structure are different from those described by Wade and Chidsey.[67] The triangular regions here are large, of the order of $1 \mu m$, and were most likely created during the polishing process. Some other factors that differentiate this batch from others are larger concentration of dopant and minimal (undetectable) miscut. While etching may be accelerated at the dopant sites, surfaces with a finite miscut may be macroscopically stabilized during etch.

2. Batch A, x-ray reflectivity

X-ray synchrotron measurements were taken in a horizontal scattering plane using x rays of wavelength $\lambda = 1.563$ Å. Schematic representation of the scattering geometry is shown in Fig. 10. Horizontal slit opening for the measurements shown here was 2.5 mm, vertical slit opening 3 mm. The distance from the sample to the detector slit was measured to be 437 mm. The effective coherence length in this measurement along the substrate (axis x in Fig. 10) is determined primarily by the detector resolution.

$$2\pi/\xi_x = \frac{2\pi}{\lambda}\delta\beta\sin\beta = \frac{1}{2}q_z\delta\beta, \qquad (20)$$

where $\beta = \alpha$ in reflectivity geometry. For the detector horizontal slit opening of 2.5 at 437 mm distance from the sample, the detector resolution $\delta\beta$ is ≈ 5.7 mrad, and the coherence length in the scattering plane ξ_x varies from
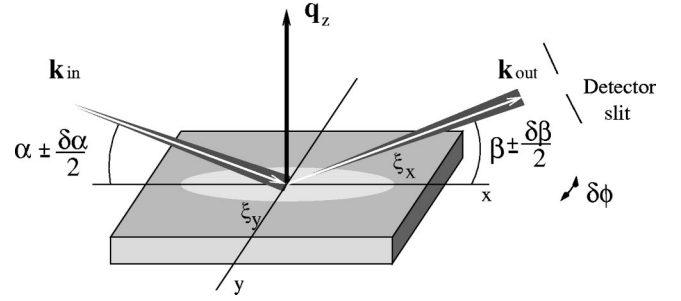

FIG. 10. Schematic representation of the x-ray scattering geometry. The nominal wave vector transfer along the surface normal is $q_z = 2\pi/\lambda(\sin\alpha + \sin\beta)$. In specular reflectivity measurements $\alpha = \beta$. Actual measurements are performed in the horizontal scattering plane, with a vertical substrate surface. The effective coherence area, $\xi_x \times \xi_y$, is determined by the uncertainties in the wave vector transfer projected onto the substrate surface.

0.22 μm at $q_z = 1$ Å^{-1} to 7.0 μm at the critical wave vector transfer $q_c = 0.0317$ Å^{-1}. In the transverse (out of plane of scattering) direction, the coherence length ξ_y is independent of the incident angle and is of the order of $\xi_y = \lambda/\delta\phi \approx 270$ Å for the 2.5 mm vertical slit opening.

A plot of the reflectivity for substrate A normalized to the ideal (Fresnel) reflectivity is given in Fig. 11. The data between $q_z = 0.1$ Å^{-1} and $q_z = 0.5$ Å^{-1} is consistent with a model where the effective roughness is a function of the wave vector transfer q_z: $\sigma_{eff}^2 = 1.53 q_z^{-1}$ Å^2. One would expect such behavior given that the surface is locally flat and the effective roughness is caused by the increase in height variations between two points with increasing separation between the points. Since the effective coherence length scales
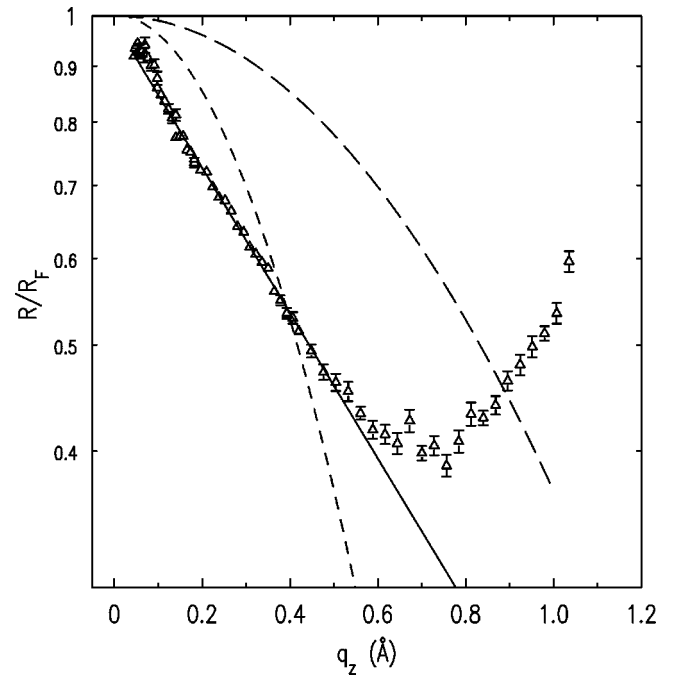

FIG. 11. Normalized reflectivity for substrate A. ($\triangle$) Substrate A normalized reflectivity. (—) Model with q_z-dependent roughness described in the text: $R/R_F = e^{-1.53 q_z}$. (– – –) Model with Gaussian roughness $\sigma = 1$ Å: $R/R_F = e^{-q_z^2}$. (- - - -) Model with Gaussian roughness $\sigma = 2$ Å: $R/R_F = e^{-4 q_z^2}$.
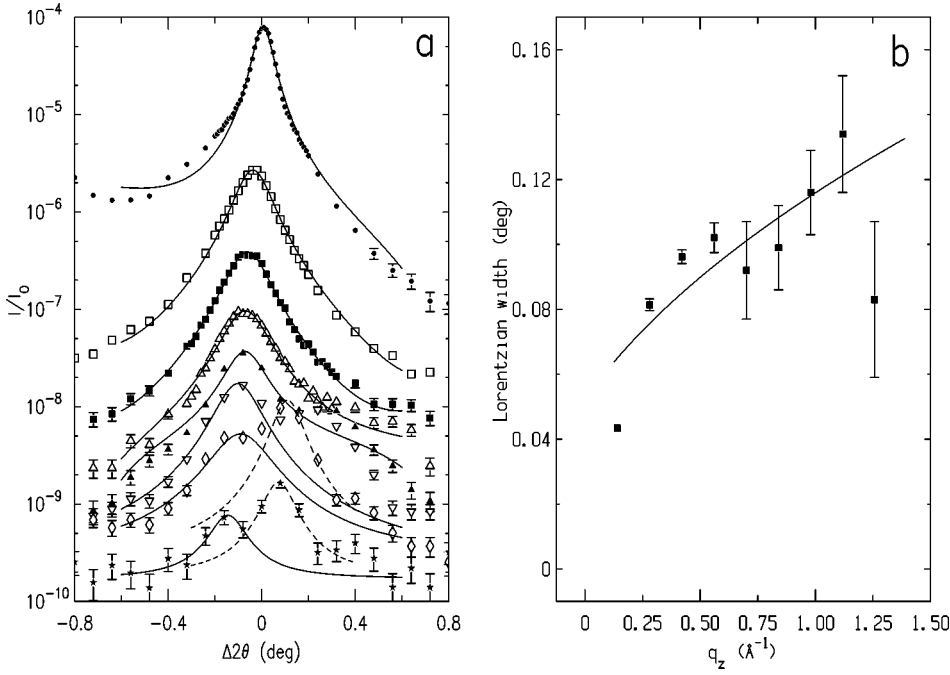
FIG. 12. (a) Spectrometer 2θ scans for incident angles $\alpha = 1° - 6°$, $8°$. Solid lines are fits to Lorentzians for the primary specular direction. Dashed lines for $6°$ and $8°$ data are fits to Lorentzians for the secondary peak (see text). (b) Lorentzian width for primary peaks vs nominal q_z. Solid line is an estimate based on the model described in the text.

as $\xi_x \propto q_z^{-1}$, the area over which the height variations are averaged decreases with increasing q_z. In terms of the coherence length from Eq. (20),

$$\sigma_{\text{eff}}^2 = 7.0 \times 10^{-4} \xi_x \text{ Å}. \tag{21}$$

This model is represented by the solid line in Fig. 11. X-ray reflectivity shows that this dependence breaks down for q_z larger than ≈ 0.5 Å^{-1} (ξ_x shorter than ≈ 450 Å), where the reflectivity approaches the ideal Fresnel reflectivity, a manifestation of a locally flat surface. Some deviation is also evident for q_z smaller than ≈ 0.1 Å^{-1} (ξ_x longer than ≈ 2 μm), where macroscopic polishing limits the height variations. The roughness measured by AFM (Fig. 9) corresponds to a length of ≈ 6.5 μm.

Apart from altering the specular reflectivity, local variations in the surface height lead to broadening of the specular peak. The illuminated area of the substrate, or the footprint, is significantly larger than the coherence area defined above. Because of the height variations, the local specular directions defined by the average planes drawn through the coherence areas will have some stochastic distribution around the specular direction defined on the length scale of the footprint. Coherent specular signals from locally defined surfaces will add up to a near-specular signal for the *average* surface. An estimate of the width of the specular peak in the regime where such scattering dominates can be inferred from Eqs. (21) and (20),

$$\Delta 2\theta \approx 2K \times \frac{\sigma_{\text{eff}}}{\xi_x} = 2K \times \sqrt{\frac{7.0 \times 10^{-4}}{\xi_x}} = 0.015 K \sqrt{q_z \delta\beta}, \tag{22}$$

where the constant K is of order 1. The detector arm (2θ) scans are performed by varying the position of the detector without moving the substrate, i.e., $2\theta = \alpha + \beta$, and α is kept constant. The plot in Fig. 12(a) shows characteristic 2θ scans for substrate A. The plot also shows Lorentzian fits to the data. The Lorentzian width parameters are plotted in Fig.

12(b). For these measurements, detector slit width was set at 0.4 mm, which corresponds to $\delta\beta$ of 0.92 mrad, or $0.052°$. An estimate of the width of the specular signal from Eq. (22) with constant $K = 4$, convoluted with the detector resolution, is shown as a solid line in Fig. 12(b). As was the case in the analysis of the specular reflectivity, data at $q_z \lesssim 0.1$ Å^{-1} and at the largest q_z is not adequately described by this model.

Detector (2θ) scans also show development of a second peak which is offset with respect to the primary (reflectivity) peak. The position of the peak appears to be at constant $q_x = k(\cos\beta - \cos\alpha)$, which corresponds to a periodic in-plane structure on a length scale of $2\pi/q_x \approx 4000$ Å $= 0.4$ μm.

3. Batch B, SEM and AFM

The substrates used in most of the measurements described below were 3.175 mm thick (111) wafers supplied by Semiconductor Processing, Inc.[64] Preliminary measurements on the substrates included scanning electron microscope (SEM) and AFM imaging.

SEM and AFM images are shown in Figs. 13–15. The images show several notable features. There are lines indicating miscut terrace edges. No obvious features can be seen on length scales larger than ≈ 1000 Å, although the 2D fast fourier transform (FFT) of the SEM (Fig. 14) indicates Fourier components present corresponding to larger length scales. One has to note that for both SEM and AFM measurements the substrate had to be exposed to air for extended periods of time, whereas x-ray measurements are performed on substrates which are promptly and carefully evacuated upon chemical treatment.

The miscut for this batch was measured by comparing the x-ray reflectivity direction with the direction of the (111) peak. Measuring the offset for two orientations of the substrate, the direction of the miscut and its magnitude could be determined. The miscut was found to be $0.57 \pm .01°$; the direction was found to be $47 \pm 2°$ from the long axis (when mounted in the cryostat, the plane of incidence was along the long axis). The miscut angle calculated from the step size in
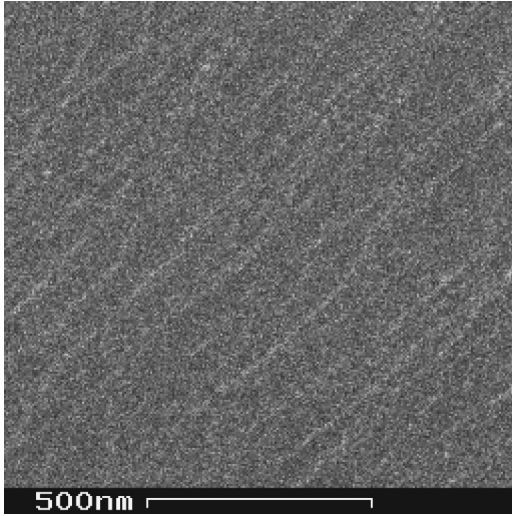
FIG. 13. SEM image of a substrate from batch B. The image was taken after chemical treatment and brief (30 min) exposure to air.

the AFM image (Fig. 15), assuming each step to be a single layer, is $\approx 0.54°$. Unfortunately, with the AFM height resolution at the signal/noise limit, the image is too noisy to produce a meaningful FFT.

4. Batch B, x-ray reflectivity

A plot of reflectivity measurements on a dry substrate from Batch B taken after the cell was cooled to $T = 20$ K is shown in Fig. 16(a). As discussed previously, the interpretation of x-ray reflectivity data has inherent ambiguities. The various fits shown on the plot illustrate this point. Real density profiles for several models with which the data is indeed consistent are displayed in Fig. 16(b).

(1) Simple Gaussian roughness [Fig. 16(1)]. Typically, substrates as delivered can be adequately represented as having a single interface with simple Gaussian roughness

$$\frac{d\rho}{dz} = \frac{\rho_{Si}}{\sqrt{2\pi}\sigma} e^{-z^2/2\sigma^2} \qquad (23)$$
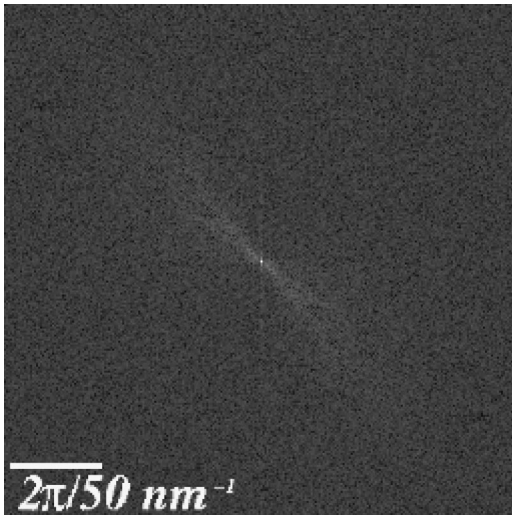

FIG. 14. Fast Fourier transform of the batch B SEM image shown in Fig. 13.

and sometimes having a native oxide layer several Å thick. With chemically treated substrates the oxide layer does not exist, and local roughness is reduced substantially. Reflectivity data is clearly no longer consistent with a Gaussian distribution at the interface. (2) An interface with an additional surface layer [Fig. 16(2)]. The data is indeed consistent with a model where both interfaces have Gaussian roughness. However, the density of such a layer would have to be $\rho = 0.04\rho_{Si}$, which can not be physically justified. If one were to use such a model in further helium film reflectivity analysis, the asymmetry in the substrate/helium interface would require an unjustified introduction of asymmetric contribution to the helium-vapor interface. In the analysis reported by Lurio et al.,[33,42,41] a similar anomaly in the bare substrate reflectivity was attributed to a layer of hydrocarbons. Although this would not alter the perceived width of the helium-vapor interface, the inferred asymmetry of that interface may be questioned.

(3) A single interface with a density distribution which falls off slower in the tails. A function with such behavior is a hyperbolic secant

$$\frac{d\rho}{dz} = \frac{\rho_{Si}}{\pi s} \operatorname{sech} \frac{z}{s}. \qquad (24)$$

The asymptotic behavior of this function is $\exp(-|z/s|)$, slower than the Gaussian. The fit to this model is satisfactory [Fig. 16(3)], and introduces only a single parameter s. Interpretation of this model, however, is not unambiguous. The first possibility is that the distribution is local, i.e., the distribution does not change with varying q_z in the measurement range. The second possibility is that the shape of the distribution is not local, and is caused by a varying coherence area due to changing q_z. The validity of such a model is supported by the analysis of batch A substrates and by the presence of large lengthscale components in the Fourier transform of the SEM image (Fig. 14). The fit to the data can be presented in terms of q_z-dependent effective Gaussian roughness σ_{eff}

$$\frac{\rho_{Si}}{\sqrt{2\pi}\sigma_{eff}} e^{-z^2/2\sigma_{eff}^2} = \frac{\rho_{Si}}{\pi s} \operatorname{sech} \frac{z}{s}. \qquad (25)$$

The plot of σ_{eff} vs q_z is shown in Fig. 16(c).

In summary of this section, silicon wafers used in helium film measurements were processed to produce locally flat surfaces. SEM and AFM imagery complemented x-ray specular reflectivity and near-specular measurements to develop a complete and consistent understanding of the substrate surface structure. This understanding is crucial to the interpretation of x-ray data on helium films in the interference geometry.

V. EXPERIMENTAL SETUP

A. X-ray scattering

X-ray measurements were performed on X22B beamline of the National Synchrotron Light Source (NSLS), Brookhaven National Laboratory (BNL). The cryostat was mounted on a two-circle x-ray goniometer, partly counterweighed to reduce the load on the motorized rotation stage.
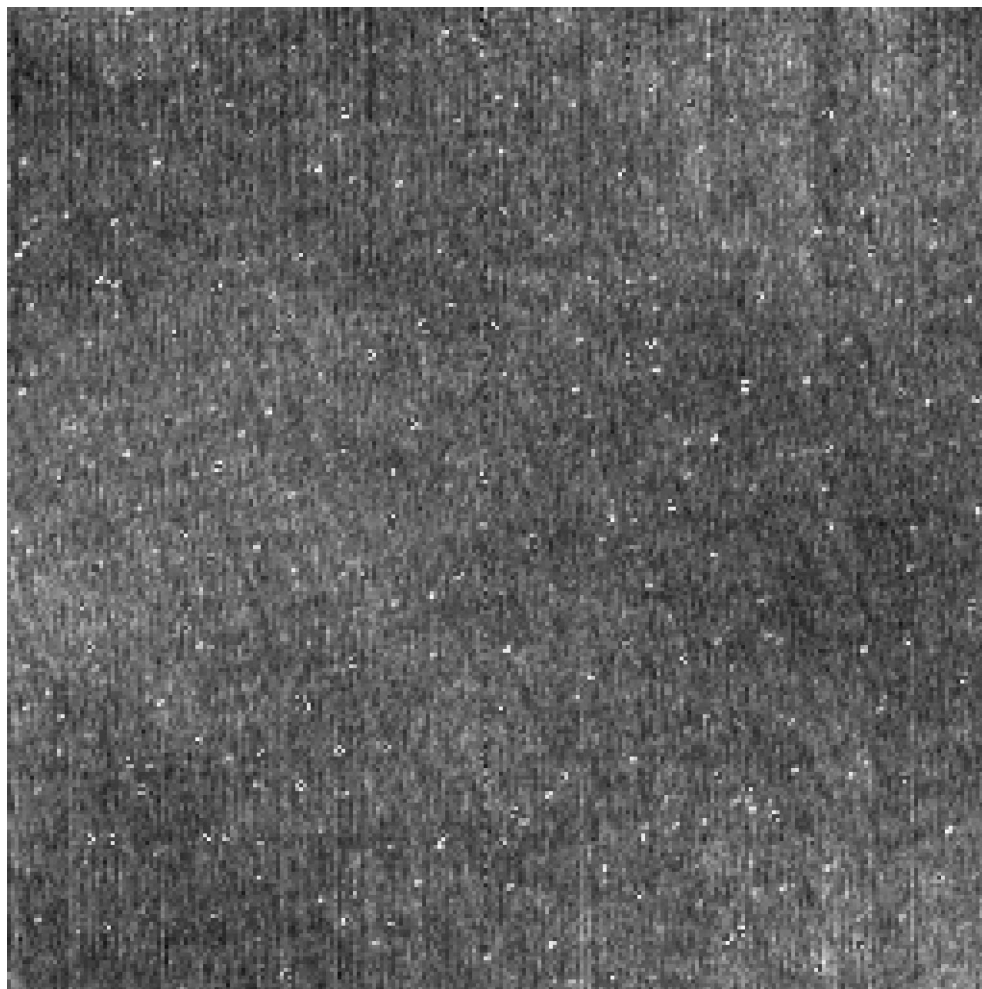
FIG. 15. AFM image of a batch B substrate. Image size is $10~\mu m \times 10~\mu m$. The r.m.s. height variation over the entire image is 3.26 Å. The height variation is 80 Å. Direction of the miscut terraces is different from that on the SEM image (Fig. 13) due to a different mounting angle. The image was taken while the wafer was exposed to air.

A schematic horizontal cross-section of the scattering setup is shown in Fig. 17. The calibrated attenuator (i) was needed to insure that the photon flux remained within the linear dynamic range of the detector (i.e., $\lesssim 30000$ cts./sec.).

B. Cryostat and insert

The general design of the cryostat used in the measurements has been described in detail elsewhere.[33,42,41] The cryostat is of vapor-cooled design and is equipped with x-ray transparent windows.

A schematic diagram of the insert is shown in Fig. 18. The cryostat has been rebuilt to include a ^{3}He cooling stage, which consists of a sorption pump, condenser, and ^{3}He pot. The lowest temperature achievable in the measurements was ≈ 0.45 K. The base temperature was limited by the heat leak from the 1 K pot and by the slow speed of the sorption pump, both attributable to compact design. Radiation leak through the windows was negligible. Mechanical rigidity of the cryostat is essential in the x-ray reflectivity measurements. Pressure variations in the continuous fill pot and in the evacuation line, necessary to regulate the 1 K pot temperature, introduce variable torque on the lower part of the insert. To avoid uncontrolled twisting of the cell, a centering

plate was used to clamp the lower insert. The problem was also mitigated in the measurements at cell temperatures below 1 K, during which the 1 K pot was evacuated to pressures $\lesssim 1$ Torr and no pressure control was necessary.

C. Temperature measurement and control

Temperature control was achieved by a feedback loop based on the signal from a germanium thermometer mounted on the cold plate to which the cell is attached. To extend the running time at elevated temperatures, the sorption pump temperature was also controlled. Typical running time at $T = 0.5$ K was of order 5 h, while a typical reflectivity measurement took 2 h.

When taking data on thick undersaturated films at temperatures above 1 K, it was important to maintain temperature stability throughout the measurements because of the strong dependence of film thickness on temperature. Variations in thickness due to temperature drift would contribute to measured roughness and thus would compromise the data analysis. In contrast, at temperatures below 0.65 K the amount of helium in the vapor was negligible and there was no measurable film thickness change between 0.45 and 0.65 K. Temperature stability during the measurements was main-
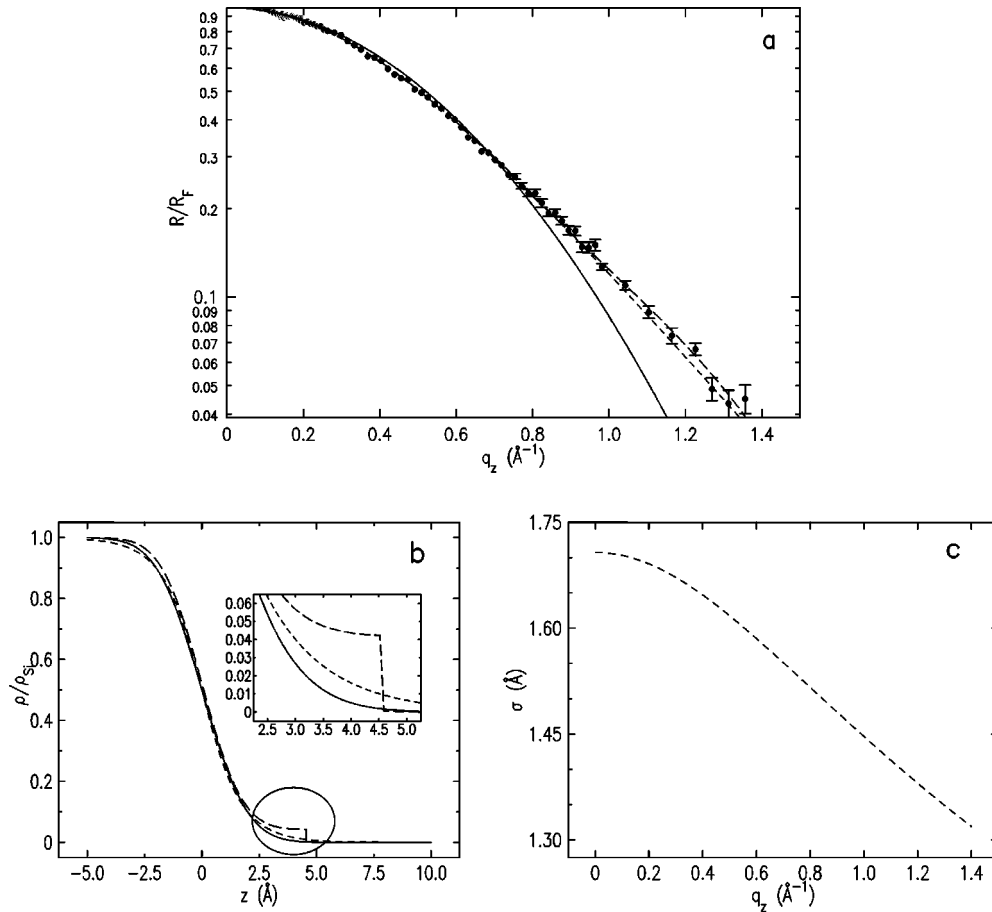
FIG. 16. X-ray reflectivity for a batch B substrate (●) and fits to models 1–3: (1) (—) Single interface with Gaussian roughness σ = 1.554 Å. (2) (– – –) A film of thickness d = 4.56 Å and density ρ = 0.0417ρ_{Si} with Gaussian roughnesses for both interfaces: $\sigma_{sub/film}$ = 1.39 Å, $\sigma_{film/vacuum}$ = 0. (3) (----) Single interface with hyperbolic secant profile of width s = 1.087 Å. (a) Reflectivity data normalized to Fresnel reflectivity and fits of several models to the data. (b) Real-space density profiles for the selected models assuming uniform profiles. Circled area of the plot is magnified in the inset. (c) Gaussian width σ vs q_z for a model with a single Gaussian interface, where functional dependence of $\sigma(q_z)$ is based on fit (3).

tained to within 1 mK, sufficient to eliminate any contribution to the apparent roughness from the temperature drift.

The accuracy of absolute temperature measurement was limited by the quality of secondary calibration to 5%. The calibration was checked at the helium λ point by a heat capacity measurement.

D. Experimental cell

The experimental cell (Fig. 19) consists of copper lid and body, with an indium seal. To keep the cell evacuated when outside the cryostat, a valve which can operate at low temperatures (i) is mounted on top of the lid. A narrow stainless steel capillary (ID of 0.3 mm, or 0.012 in.) fill line (k) is attached to the valve with an indium flange assembly. The lid also features two high voltage feed throughs (j) and a removable Kapton membrane capacitance pressure gauge. The substrate holder (Fig. 6) is attached to the lid from below. X-ray transparent beryllium windows (2.5 mm, or 0.1 in. thick)(e) capable of withstanding the helium solidification pressure of 25 bar are attached to the cell body by indium seals and clamped with stainless steel clamps.
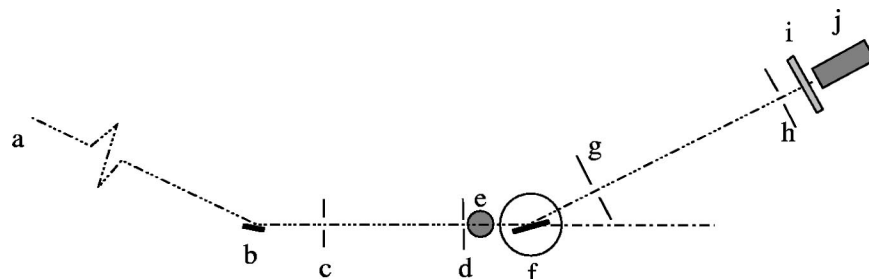

FIG. 17. Schematic representation of the scattering geometry. (a) synchrotron source; (b) Ge (111) monochromator; (c) background slit; (d) incident defining slit; (e) beam monitor; (f) cryostat, sample cell and Si (111) substrate on the θ stage; (g) output background slit; (h) detector slit; (i) calibrated attenuator; (j) detector.
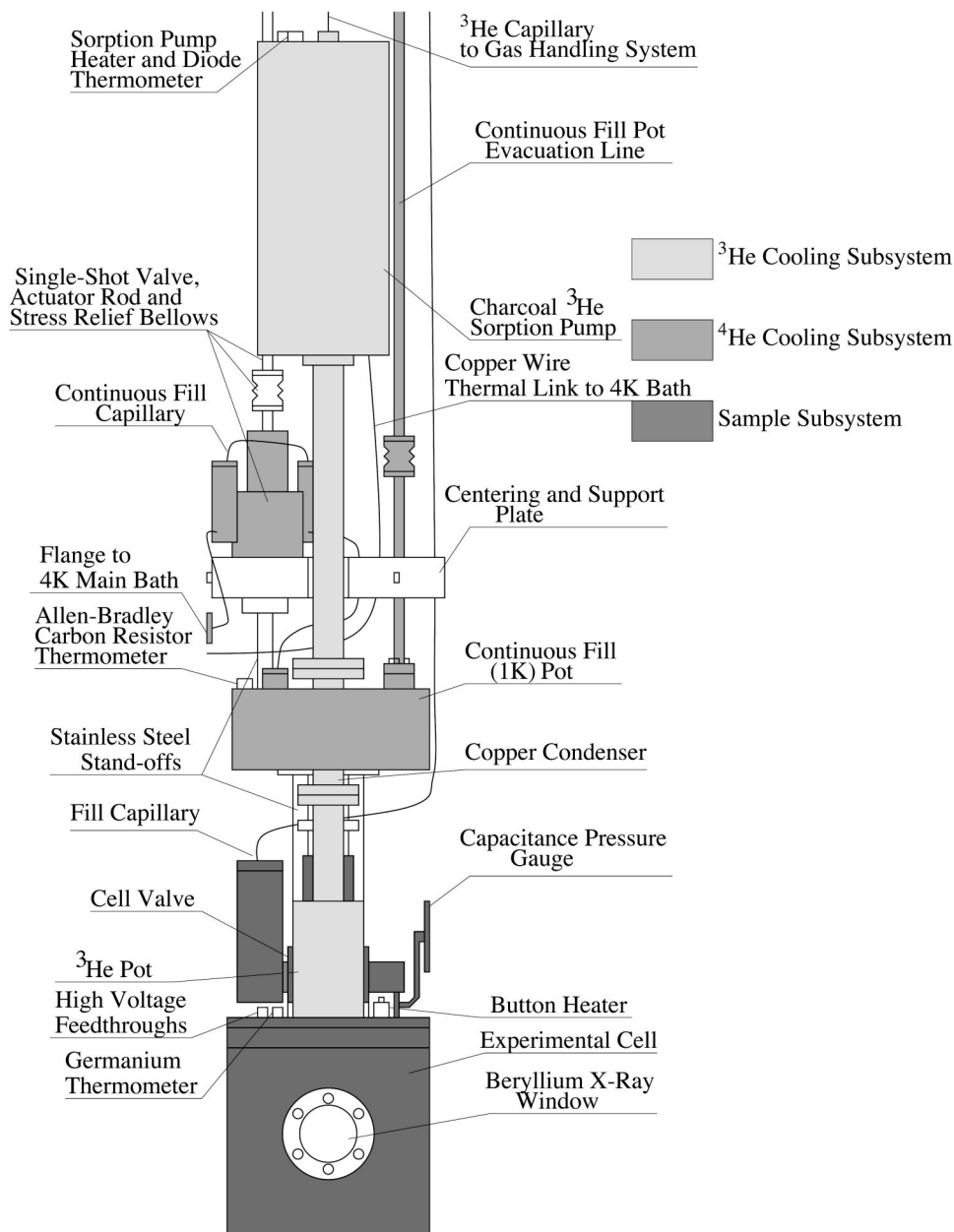
FIG. 18. Schematic diagram of the lower cryostat insert.

After the substrate was mounted inside the cell and the cell was evacuated, it was attached to the ^{3}He stage and to the fill line capillary. Following this, the cryostat was closed.

VI. DATA ACQUISITION

A comprehensive collection of data was obtained for different temperatures and film thicknesses. The temperature-thickness coordinates for all available data are presented in Fig. 20. Most of the data was taken in two temperature bands (low temperature A and high temperature B), mostly because the cryostat handling and temperature control were more reliable near the base temperature of the ^{3}He pot (A) and of the 1 K continuous fill pot (B). The thickness of the undersaturated films in region A was changed by introducing helium into the cell in small doses. In region B, where the ^{4}He vapor pressure becomes significant, thickness is a strong function of temperature and can be controlled by either varying the temperature or by changing the dosage. Although a

capacitance pressure gauge capable of measuring pressure *in situ* was built and tested, it was removed in the final measurements because the Kapton membrane in the gauge allowed small amounts of helium to diffuse into the cell during the cryostat cool down.

To remove helium from the cell, the bottom part of the insert was heated to ≈ 70 K while the cell was evacuated. Testing for any residual helium was done by comparing reflectivity curves at $T=20$ K and $T=0.45$ K after evacuation.

Reflectivity data was taken by measuring detector [Fig. 17(j)] and beam monitor (e) counts at a set of incident angles θ and detector arm positions 2θ. For each reflectivity angle the specular signal was taken, where $2\theta=2\times\theta$. The off-specular (background) signal was measured at $2\theta=(2\times\theta)\pm\Delta$ where the offset Δ was set somewhat arbitrarily at $0.2°$. At several θ values, 2θ scans were performed to ascertain the proper alignment and to make sure that the value of Δ is set properly. A typical 2θ scan set is shown in Fig. 21. In
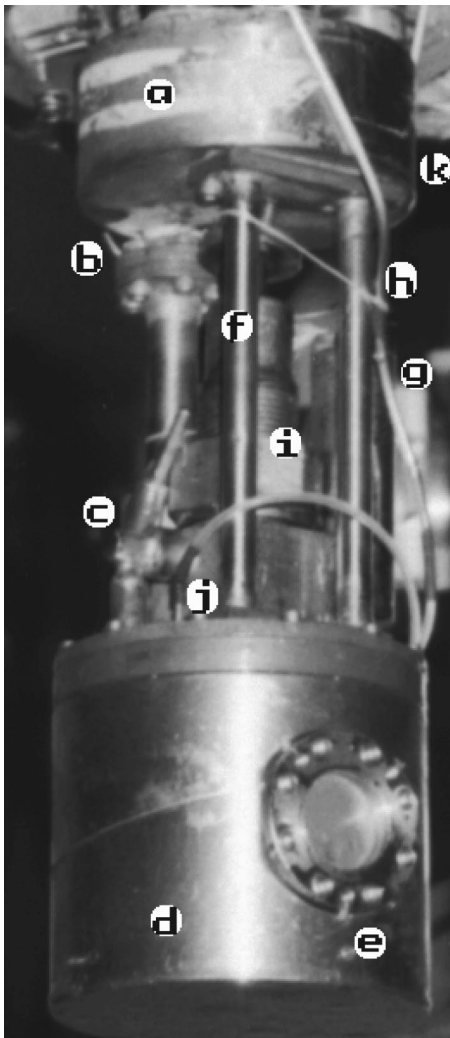
FIG. 19. Lower insert. (a) 1 K pot; (b) condenser; (c) ³He pot; (d) cell; (e) beryllium window assembly; (f) structural support; (g) fill line connector; (h) high voltage wire; (i) valve; (j) high voltage feed-through; (k) fill capillary.

FIG. 20. Temperature-thickness plot of available data for ⁴He films. Each point represents a reflectivity data set. Regions A and B constitute low- and high-temperature regimes discussed in the analysis.

VII. DATA ANALYSIS

A. Surface profile models and length conventions

The surface profiles for the helium surface presented by both theoretical and experimental studies vary in their functional form. Variational methods give numerical solutions which cannot usually be presented in closed functional form. Common choices for parametrized models in density functional models and experimental results are the Fermi function,[34] the generalized Fermi function,[7,11] and the hyperbolic secant.[33,42,41]

For meaningful comparison of various results, it is common to denote the length scale over which the density changes from 90% of the bulk value to 10% as the interfacial width t. In this work, the interfaces are parametrized by ei-

contrast with batch A substrate 2θ scans (Fig. 12), the increase in width of these scans with increasing θ is negligible in comparison with the width defined by the detector slit. The main sources of the background signal are small angle x-ray scattering from the cryostat windows and from the air in the beam path.

The reflectivity signal was computed by subtracting the average background obtained from both sides of the specular peak in 2θ scans. The computed counts were then normalized to the direct beam taking into account the attenuation of the absorber wheel.

An example of the resultant raw background subtracted reflectivity data is shown in Fig. 22. The reflectivity data spans several orders of magnitude. To discern its details with more precision, and to be able to compare the data with the ideal Fresnel reflectivity [Eq. (15)], the data is normalized to the expected silicon Fresnel reflectivity. Normalized low-temperature data is presented in the next section (see Fig. 24).
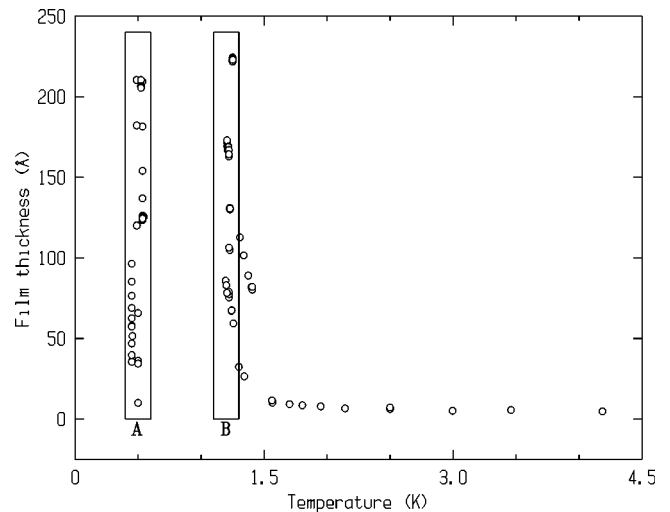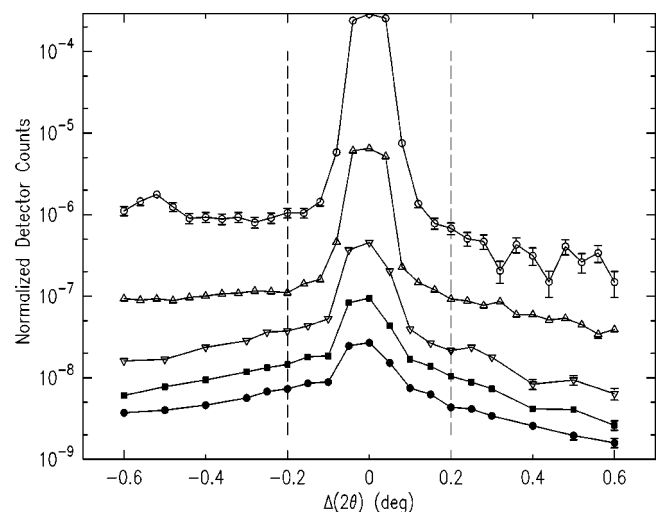

FIG. 21. Detector (2θ) scans for a set of nominal θ and corresponding q_z for a typical reflectivity set. Vertical lines indicate the offset Δ at which data for background subtraction was taken. ($\bigcirc$) $\theta = 0.7°$, $q_z = 0.123$ Å^{-1}; ($\triangle$) $\theta = 1.7°$, $q_z = 0.298$ Å^{-1}; ($\bigtriangledown$) $\theta = 3.0°$, $q_z = 0.526$ Å^{-1}; ($\blacksquare$) $\theta = 4.0°$, $q_z = 0.702$ Å^{-1}; ($\bullet$) $\theta = 5.0°$, $q_z = 0.877$ Å^{-1}.
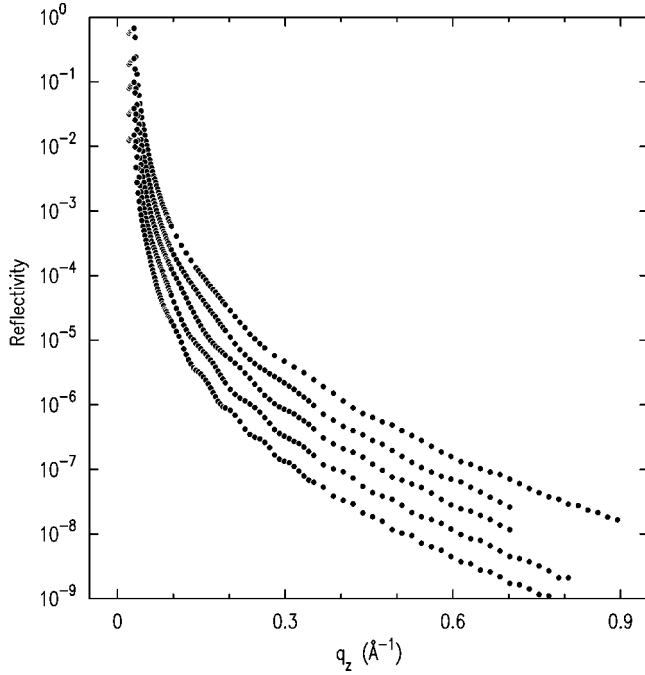
FIG. 22. Plot of raw reflectivity for a subset of low-temperature data. Data sets are offset for clarity. Differences in oscillation periods evident in the plots indicate different helium film thicknesses. Error bars are smaller than the symbol size. Temperatures and fitted film thicknesses for the displayed data are (top to bottom) 0.5 K, 36.1 Å; 0.45 K, 39.9 Å; 0.45 K, 57.3 Å; 0.45 K, 76.1 Å; 0.491 K, 120.2 Å.

ther a Gaussian (r.m.s.) width σ or a hyperbolic secant width parameter s. For a Gaussian interface, $t = 2.563\sigma$, whereas for a symmetric hyperbolic secant interface $t = 3.685s$. The film thickness is commonly presented in atomic layers. For
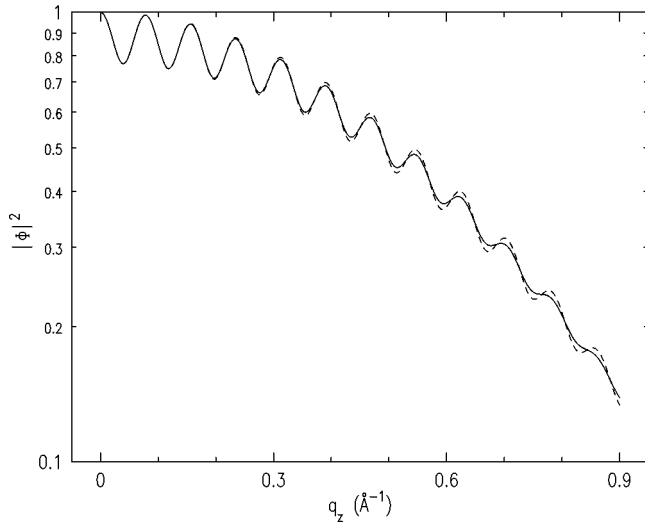

FIG. 23. Expected measured structure factor for a film with the same local (intrinsic) surface width with (—) and without (----) long-range correlations with substrate. Long-range substrate surface height variations add to the local surface width if the film conforms to the substrate surface. This results in a more rapid decay of the interference oscillations. In the analysis of reflectivity from conformal surfaces the assumption that the interfaces are not correlated would result in overestimated surface width.
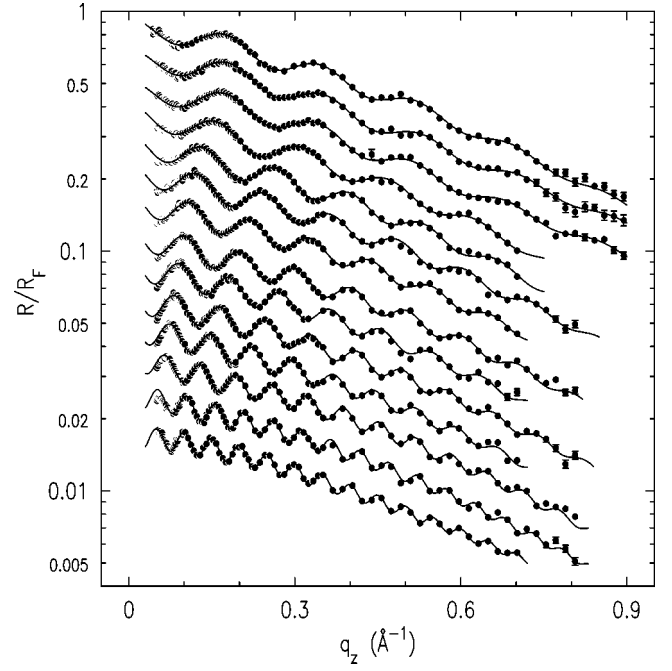

FIG. 24. Reflectivity normalized to the Fresnel reflectivity for an ideal Si substrate for low-temperature data. Data sets are offset for clarity. The model is described in the text. Fit parameters for each data set are listed in Table III, in the same order.

comparison with literature that uses the physical scale, one atomic layer corresponds to 3.6 Å for ^{4}He.

B. Modeling the density profile

Data obtained during synchrotron measurements was fit to a set of models. As pointed out earlier in the discussion on the substrates used, unambiguous knowledge of the substrate surface cannot be obtained by x-ray measurements alone. We can, however, extract meaningful information on the helium-vapor interface if either (a) independent non-x-ray measurements provide a reliable model for the substrate surface or (b) the substrate interfacial width is significantly smaller than the width of the helium-vapor interface, in which case precise knowledge of the origins of the substrate structure is less important.

A generalized view for models used in fitting is shown in Fig. 5. The system is represented by a series of slabs. Each slab is characterized by its width d and density ρ. The interfaces are characterized in this case by their Gaussian widths σ: $d\rho/dz \propto e^{-z^2/2\sigma^2}$. For this model, the structure factor

$$\Phi(q_z) = \frac{1}{\rho_{Si}} \int_{-\infty}^{\infty} \left(\frac{(\rho_{Si} - \rho_{He})}{\sqrt{2\pi}\sigma_{Si\text{-}He}} e^{-z^2/2\sigma_{Si\text{-}He}^2} \right.$$

$$\left. + \frac{\rho_{He}}{\sqrt{2\pi}\sigma_{He\text{-}vac}} e^{-(z-d_{He})^2/2\sigma_{He\text{-}vac}^2} \right) e^{iq_z z} dz$$

$$= \frac{\rho_{Si} - \rho_{He}}{\rho_{Si}} e^{-q_z^2 \sigma_{Si\text{-}He}^2/2} + \frac{\rho_{He}}{\rho_{Si}} e^{-q_z^2 \sigma_{He\text{-}vac}^2/2} e^{iq_z d}.$$

$$(26)$$

In more sophisticated models additional features are added to the density profile. The Gaussian shape with roughness σ can be replaced either by a hyperbolic secant with width s $[d\rho/dz \propto \text{sech}(z/s)]$, convolution of such with Gaussian roughness, or sum of the two with various weights. The roughness of the substrate can also be q_z dependent (see Sec. IV D 4 above). The models can be further modified by adding additional layers. Although the reflectivity data is not invertible and the real density profile can not be determined uniquely, the simplest physically justified model is generally a good guide to the physical profile.

C. Conformal vs nonconformal roughness

Analysis of the substrate x-ray, SEM, and AFM data (Sec. IV B) suggests that the substrate is locally flat, with overall roughness dominated by the miscut. Since the miscut terrace size is of the order of 350 Å, which is larger than the typical film thickness, the helium surface would conform to the substrate surface.[68–70] The two interfaces cannot be treated as independent. Instead, the local structure needs to be convoluted with the substrate roughness. Equation (26) is then modified as follows:

$$\Phi(q_z) = e^{-q_z^2 \sigma_{\text{Si}}^2/2} \left(\frac{\rho_{\text{Si}} - \rho_{\text{He}}}{\rho_{\text{Si}}} + \frac{\rho_{\text{He}}}{\rho_{\text{Si}}} e^{-q_z^2 \sigma_{\text{He-vac}}^2/2} e^{iq_z d} \right).$$
(27)

Figure 23 shows the expected R/R_F for a helium film 80 Å thick with a 2 Å *local* Gaussian roughness on a substrate which has 1.5 Å Gaussian roughness without correlation as well as with perfect correlation. As shown by Eq. (27), *any* representation of the substrate surface that adequately describes x-ray reflectivity of the substrate can be used to describe this model with conformal roughness. A data set analyzed by a model which does not account for film-substrate correlations where they exist would result in overestimated surface width.

D. Solid helium layer

Van der Waals helium-substrate interaction for films thicker than some minimum value leads to a local pressure near the substrate surface that is larger than that near the free surface, or in the vapor. Estimates from the helium equation of state and the melting curve[71] indicate that the local helium density reaches solidification pressure at a distance of order 4 Å from the substrate for films thicker than ≈ 10 Å. Proximity of a hard wall and changes to the simple Lennard-Jones potential at smaller distances makes precise determination of the local density profile a problem in itself.[53,6,72] X-ray specular reflectivity is consistent with a rough layer which is 2–6 Å thick with density in the range $0.1\rho_{\text{Si}}$ to $0.14\rho_{\text{Si}}$, the two parameters being strongly correlated, but not influencing the helium-vapor width.

E. Thick films

Lurio *et al.*[33,42,41] noted that under certain circumstances the contrast of reflectivity oscillations was significantly reduced. We found similar reduction for all thick films, not only saturated films. We attribute the attenuation to the long wavelength standing third sound waves driven by acoustic vibrations in the building.

In view of theoretical predictions of the spatial dependence of the conformal coupling it is not clear the assumptions essential to conformal roughness are valid for thicker films. In the data analysis, only data on films up to 130 Å thick is used.

F. Modified theoretical model and fitting

The model used to fit the reflectivity data follow the considerations described above. The model for the local density profile included a perfectly sharp silicon–solid-helium interface, a thin solid helium (sHe) layer and a liquid helium film. The helium-vapor interface was modeled by a symmetric hyperbolic secant. Fits in which a Gaussian profile was substituted yield somewhat larger χ^2, although the difference was not statistically significant. Typically, somewhat smaller (by 5–10 %) 10%/90% widths were obtained if the Gaussian profile was used. The hyperbolic secant profile was selected because most of the theoretical studies suggest exponential rather than Gaussian asymptotic behavior.

Since we are treating the two interfaces as conformal, the local density profile is convoluted with the substrate density profile. Because the structure factor is obtained by taking a Fourier transform of the profile derivative, and because Fourier transform of a convolution of two functions is a product of individual Fourier transforms, a hyperbolic secant substrate profile and a Gaussian substrate profile with a q_z-dependent width [see Eq. (25)] both give the same result:

$$\Phi(q_z) = \text{sech}\left(\frac{\pi s_{\text{Si}} q_z}{2} \right) \left[\frac{\rho_{\text{Si}} - \rho_{s\text{He}}}{\rho_{\text{Si}}} \right.$$

$$+ \frac{\rho_{s\text{He}} - \rho_{\text{He}}}{\rho_{\text{Si}}} e^{-q_z^2 \sigma_{s\text{He-He}}^2/2} e^{iq_z d_{s\text{He}}}$$
(28)

$$+ \left. \frac{\rho_{\text{He}}}{\rho_{\text{Si}}} \text{sech}\left(\frac{\pi s_{\text{He}} q_z}{2} \right) e^{iq_z(d_{s\text{He}} + d_{\text{He}})} \right]$$
(29)

In the fitting procedure, the parameters s_{Si}, $\rho_{s\text{He}}$, $\sigma_{s\text{He-He}}$, $d_{s\text{He}}$, ρ_{He}, s_{He}, and d_{He} were allowed to vary. In addition to these, the intensity normalization factor was fit as well.

Typical χ^2 values achieved during fitting were 1.05–1.6. For thinner films, confidence limits for s_{He} were calculated by χ^2 minimization for a set of constant s_{He} around the best fit value while allowing other parameters to float. For thicker films, a spectral noise analysis procedure similar to that used by Lurio *et al.*[41,42] was employed. Error bars in the reported data correspond to 66% confidence limits.

G. Low-temperature data

A subset of data from region A in diagram 20 is displayed in Fig. 24. Also shown are fits to the model in Eq. (28). The total film thickness $d_{s\text{He}} + d_{\text{He}}$ and the corresponding surface profile width for the these data sets are shown in Table III.

TABLE III. Fit parameters for low temperature data sets (Fig. 24). The total film thickness is the sum of solid layer and liquid layer thicknesses $d_{s\text{He}}+d_{\text{He}}$. Parameter $s_{\text{He/vapor}}$ is the hyperbolic secant width of the helium/vapor interface; $t_{\text{He/vapor}}$ is the corresponding 10%/90% width. The typical error in $d_{s\text{He}}+d_{\text{He}}$ is ±1.5 Å.

$d_{s\text{He}}+d_{\text{He}}$, Å	T, K	$s_{\text{He/vapor}}$, Å	$t_{\text{He/vapor}}$, Å
36.1	0.500	1.45±0.13	5.34±0.48
35.5	0.450	1.45±0.19	5.34±0.7
36.7	0.455	1.45±0.16	5.33±0.59
39.9	0.450	1.51±0.13	5.56±0.48
47.1	0.450	1.45±0.11	5.34±0.41
51.5	0.455	1.58±0.16	5.82±0.59
57.3	0.450	1.66±0.11	6.12±0.41
62.3	0.450	1.55±0.12	5.71±0.44
68.7	0.450	1.76±0.20	6.49±0.74
76.1	0.450	1.62±0.13	5.97±0.48
84.7	0.450	1.74±0.15	6.41±0.55
96.9	0.450	1.42±0.12	5.23±0.44
120.2	0.491	1.59±0.17	5.84±0.63
125.5	0.546	1.77±0.12	6.5±0.44

H. High-temperature data

A subset of data from region B on diagram 20 is displayed in Fig. 25 and in Table IV.

I. Data summary

A plot of interface width vs thickness for both low and high temperature data is shown in Fig. 26.

TABLE IV. Fit parameters and temperature for high-temperature data.

$d_{s\text{He}}+d_{\text{He}}$, Å	T, K	$s_{\text{He/vapor}}$, Å	$t_{\text{He/vapor}}$, Å
59.25	1.256	2.02±0.2	7.44±0.74
67.02	1.244	1.82±0.2	6.71±0.74
75.16	1.222	2.17±0.18	8.00±0.66
78.37	1.212	1.77±0.2	6.52±0.74
78.87	1.220	2.16±0.18	7.96±0.66
85.76	1.195	2.03±0.2	7.48±0.74
83.25	1.200	2.14±0.17	7.89±0.63
105.0	1.228	2.05±0.38	7.53±1.4
106.9	1.222	2.21±0.3	8.14±1.1
130.6	1.229	2.39±0.3	8.81±1.1
130.0	1.230	1.84±0.36	6.78±1.3
130.3	1.230	2.11±0.42	7.78±1.5

VIII. DISCUSSION AND CONCLUSION

An earlier study by Lurio et al.[33,42,41] resulted in a helium liquid-vapor interface width of 9.1 ± 1 Å, somewhat larger than predicted by theory. In that work the lowest temperature was 1.13 K, not yet in the low-temperature limit. To compare to theory which gives values at $T=0$, the data had to be corrected to zero temperature. In the present article we have studied the profile in the low-temperature limit, as well as its dependence on the helium film thickness. From Tables III and IV and Fig. 26, the 10%/90% interfacial width for temperature $T=0.45$ K varies from 5.3 ± 0.5 Å for 36 ± 1.5 Å thick films to 6.5 ± 0.5 Å for 125 ± 1.5 Å thick films. For $T=1.22$ K, the width is 7.8 ± 1.0 Å. These values for the interface width are somewhat lower than those estimated for $T=0$ by Lurio et al.[33,42,41].

The difference in the results are mainly due to interpretation of the data using Eq. (27), which followed from a better undertanding of the film/substrate system and the characterization of the substrate. Lurio et al. assumed uncorrelated substrate-helium and helium-vapor interfaces. The character
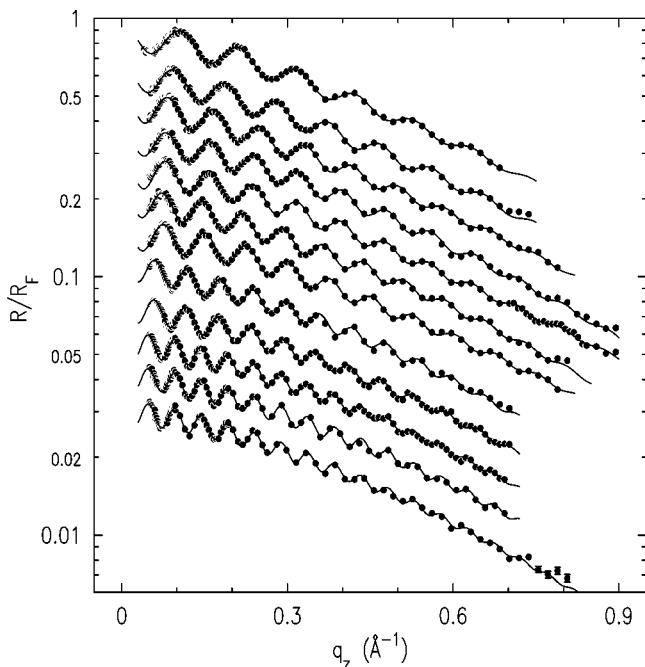

FIG. 25. X-ray reflectivity normalized to the Fresnel reflectivity for an ideal Si substrate for high temperature data. The model is described in the text. Data sets are offset for clarity. Fit parameters for each data set are listed in Table IV, in the same order.
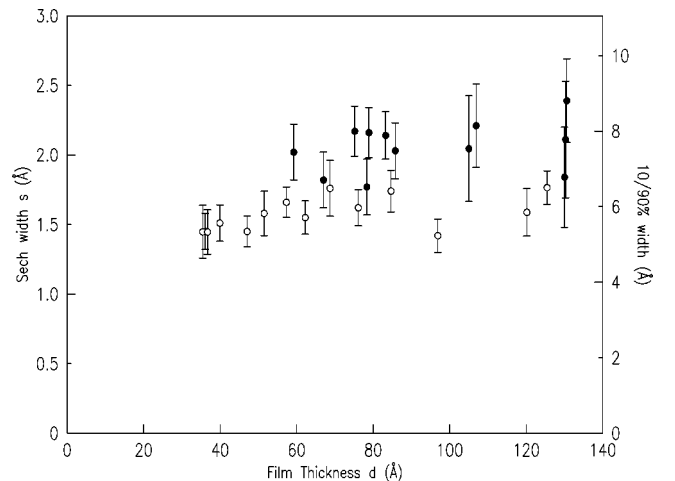

FIG. 26. Width of the helium-vapor interface for low (o) (0.45–0.55 K) and high (•) (1.195–1.256 K) temperature data. Both hyperbolic secant parameter for the helium-vapor interface s_{He} (labels on the left) and the corresponding 10%/90% width (on the right) are given as a function of total film thickness.

of x-ray reflectivity for the bare substrate[42] appears to be similar to the ones reported here. This may be an indication that large length scale components in the surface height variations existed in Lurio et al. substrates as well.

The current data does not justify the introduction of an additional parameter describing the asymmetry of the profile but certainly does not rule out such asymmetry. Thicker films and a larger q_z range would be required to make such a determination. Our results are in essential agreement with the density functional theoretical predictions of Cheng et al.[6] and Guirao[7], analytical variational calculations by Epstein

and Krotscheck,[9] and variational Monte-Carlo works of Pieper et al.[11] and Lewart et al.[12]

*Present address: UC Berkeley Physics Dept., Berkeley, CA 94720.

[1] J. Daillant, K. Quinn, C. Gourier, and F. Rieutord. J. Chem. Soc. **92**, 505 (1996).

[2] J. Als-Nielsen, in *Structure and Dynamics of Surfaces*, edited by W. Schommers and P. v. Blankenhagen (Springer, Berlin, 1987), Vol. 43.

[3] H. Tostmann, E. DiMasi, B. M. Ocko, M. Deutsch, and P.S. Pershan, J. Non-Cryst. Solids **182**, 250 (1998).

[4] V. M. Kaganer, H. Möhwald, and P. Dutta, Rev. Mod. Phys. **71**, 779 (1999).

[5] W. Brouwer and R. Pathria, Phys. Rev. **163**, 200 (1967).

[6] E. Cheng, Milton W. Cole, W. F. Saam, and Jacques Treiner, Phys. Rev. B **46**, 13 967 (1992).

[7] A. Guirao, M. Centelles, M. Barranco, M. Pi, A. Polls, and X. Viñas. J. Phys.: Condens. Matter **4**, 667 (1992).

[8] F. D. Mackie and Chia-Wei Woo, Phys. Rev. B **18**, 529 (1978).

[9] Janice L. Epstein and Eckhard Krotscheck, Phys. Rev. B **37**, 1666 (1988).

[10] C. E. Campbell, B. E. Clements, E. Krotscheck, and M. Saarela, Phys. Rev. B **55**, 3769 (1997).

[11] Steven C. Pieper, R. B. Wiringa, and V. R. Pandharipande, Phys. Rev. B **32**, 3341 (1985).

[12] D. S. Lewart, V. R. Pandharipande, and Steven C. Pieper, Phys. Rev. B **37**, 4950 (1988).

[13] S. A. Chin, J. Low Temp. Phys. **93**, 921 (1993).

[14] Akira Tamura, J. Phys.: Condens. Matter **10**, 10 135 (1998).

[15] V. U. Nayak, D. O. Edwards, and N. Masuhara, Phys. Rev. Lett. **50**, 990 (1983).

[16] J. J. Berkhout, O. J. Luiten, I. D. Setija, T. W. Hijmans, T. Mizusaki, and J. T. M. Walraven, Phys. Rev. Lett. **63**, 1689 (1989).

[17] M. J. DiPirro and F. M. Gasparini, Phys. Rev. Lett. **44**, 269 (1980).

[18] Bidyut K. Bhattacharyya, Michael J. DiPirro, and Francis M. Gasparini, Phys. Rev. B **30**, 5029 (1984).

[19] N. Alikacem, R. B. Hallock, R. H. Higley, and D. T. Sprague, J. Low Temp. Phys. **87**, 279 (1992).

[20] D. T. Sprague, N. Alikacem, P. A. Sheldon, and R. B. Hallock, Phys. Rev. Lett. **72**, 384 (1994).

[21] R. Sprik, J. T. M. Walraven, G. H. van Yperen, and Isaac F. Silvera, Phys. Rev. B **34**, 6172 (1986).

[22] A. P. Mosk, M. W. Reynolds, T. W. Hijmans, and T. M. Walraven, Phys. Rev. Lett. **81**, 4440 (1998).

[23] A. I. Safonov, S. A. Vasilyev, I. S. Yasnikov, I. I. Lukashevich, and S. Jaakkola, Phys. Rev. Lett. **81**, 4545 (1998).

[24] G. F. Saville, J. M. Goodkind, and P. M. Platzman, Phys. Rev. B **70**, 1517 (1993).

[25] C. C. Grimes, T. R. Brown, M. L. Burns, and C. L. Zipfel, Phys. Rev. B **13**, 140 (1976).

[26] H. J. Lauter, H. Godfrin, C. Tiby, H. Wiechert, and P. E. Obermayer, Surf. Sci. **125**, 265 (1983).

[27] H. J. Lauter, H. Godfrin, and H. Wiechert, in *Proceedings of the Second International Conference on Phonon Physics*, edited by J. Kollar, N. Kroo, M. Meynhard, and T. Siklos (World Scientific, Singapore, 1985), p. 842.

[28] H. J. Lauter, H. Godfrin, V. L. P. Frank, and P. Leiderer, Phys. Rev. Lett. **68**, 2484 (1992).

[29] B. E. Clements, H. Godfrin, E. Krotscheck, H. J. Lauter, P. Leiderer, V. Passiouk, and C. J. Tymczak, Phys. Rev. B **53**, 12 242 (1996).

[30] S. Balibar, Phys. Lett. **51A**, 455 (1975).

[31] A. C. Forbes and A. F. G. Wyatt, Phys. Rev. Lett. **64**, 1393 (1990).

[32] S. R. Bandler, R. E. Lanou, H. J. Maris, T. More, F. S. Porter, G. M. Seidel, and R. H. Torii, Phys. Rev. Lett. **68**, 2429 (1992).

[33] L.B. Lurio, T.A. Rabedeau, P. S. Pershan, I.F. Silvera, M. Deutsch, S. D. Kosowsky, and B. M. Ocko, Phys. Rev. Lett. **68**, 2628 (1992).

[34] D. V. Osborne. J. Phys.: Condens. Matter **1**, 289 (1989).

[35] M. W. Cole, Phys. Rev. A **1**, 1838 (1970).

[36] K. R. Atkins. Can. J. Phys. **31**, 1165 (1953).

[37] D. O. Edwards and W. F. Saam, in *Progress in Low Temperature Physics*, edited by D. F. Brewer (North-Holland, Amsterdam, 1978), Vol. VII A, p. 283.

[38] K. A. Gernoth, J. W. Clark, G. Senger, and M. L. Ristig, Phys. Rev. B **49**, 15 836 (1994).

[39] J. L. Vallés and K. E. Schmidt, Phys. Rev. B **38**, 2879 (1988).

[40] A. Griffin and S. Stringari, Phys. Rev. Lett. **76**, 259 (1996).

[41] L. B. Lurio, Ph.D. thesis, Harvard University, 1992.

[42] L. B. Lurio, T. A. Rabedeau, P. S. Pershan, Isaac F. Silvera, M. Deutsch, S. D. Kosowsky, and B. M. Ocko, Phys. Rev. B **48**, 9644 (1993).

[43] E. Krotscheck and R. Zillich, Phys. Rev. B **58**, 5707 (1998).

[44] R. B. Hallock, in *Progress in Low Temperature Physics*, edited by W. P. Halperin (Elsevier Science, British Vancouver, 1978), Vol. XIV, p. 283.

[45] K. R. Atkins and Y. Narahara, Phys. Rev. **138**, 437 (1965).

[46] A. F. Andreev, Zh. Teor. Éksp. Fiz. **50**, 1415 (1966) [Sov. Phys. JETP **23**, 939 (1966)].

[47] C. C. Chang and M. Cohen, Phys. Rev. A **8**, 3131 (1973).

[48] F. Z. Dalfovo and S. Stringari, Phys. Scr. **38**, 204 (1988).

[49] N. Pavloff and J. Treiner, J. Low Temp. Phys. **83**, 15 (1991).

[50] N. Pavloff and J. Treiner, J. Low Temp. Phys. **83**, 331 (1991).

[51] N. Pavloff and J. Treiner, Physica B **169**, 537 (1991).

[52] E. Cheng, M. W. Cole, and M. H. Cohen, Phys. Rev. B **50**, 1136 (1994).

[53] E. Cheng, Milton W. Cole, W. F. Saam, and J. Treiner, Phys. Rev. Lett. **67**, 1007 (1991).

[54] E. Cheng and Milton W. Cole, Phys. Rev. B **38**, 987 (1988).

[55] G. Deville, J. Low Temp. Phys. **72**, 135 (1988).

[56] H. M. Guo, D. O. Edwards, R. E. Sarwinski, and J. T. Tough, Phys. Rev. Lett. **27**, 1259 (1971).

[57] J. D. Jackson, *Classical Electrodynamics*, 2nd ed. (Wiley, New York, 1975).

[58] A. Braslau, P. S. Pershan, G. Swislow, B. M. Ocko, and J. Als-Nielsen, Phys. Rev. A **38**, 2457 (1988).

[59] P. S. Pershan, Synchrotron Radiat. News **12**, 10 (1999).

[60] P. S. Pershan, Phys. Rev. E **50**, 2369 (1994).

[61] J. S. Pedersen and I. W. Hamley, J. Appl. Crystallogr. **27**, 36 (1994).

[62] X.-L. Zhou and S.-H. Chen, Phys. Rev. E **47**, 3174 (1993).

[63] S. H. Chen, X. L. Zhou, and B. O. Carvalho, Prog. Colloid Polym. Sci. **93**, 85 (1993).

[64] Semiconductor Processing Corp., Boston, MA.

[65] Virginia Semiconductor Inc., Fredericksburg, VA.

[66] G. S. Higashi, Y. J. Chabal, G. W. Trucks, and Krishnan Raghavachari, Appl. Phys. Lett. **56**, 656 (1990).

[67] Christopher P. Wade and Christopher E. D. Chidsey, Appl. Phys. Lett. **71**, 1679 (1997).

[68] J. Daillant and O. Belorgey, J. Chem. Phys. **97**, 5824 (1992).

[69] J. Daillant and O. Belorgey, J. Chem. Phys. **97**, 5837 (1992).

[70] E. A. L. Mol, G. C. L. Wong, J. M. Petit, F. Rieutord, and W. H. de Jeu, Phys. Rev. Lett. **79**, 3439 (1997).

[71] J. Wilks, *Properties of Liquid and Solid Helium* (Clarendon, Oxford, 1967).

[72] D. T. Smith and R. B. Hallock. Phys. Rev. B **34**, 226 (1986).

[73] Brand-Nu Laboratories, http://www.brandnu.com